Fuel 329 (2022) 125310

Contents lists available at ScienceDirect

Fuel

journal homepage: www.elsevier.com/locate/fuel

Full Length Article

Effect of fuel temperature on flame characteristics of supersonic turbulent combustion

Jeong-Yeol Choi [a,1,*], Umesh Unnikrishnan [b,1], Won-Sub Hwang [a], Seung-Min Jeong [a], Sang-Hoon Han [c], Kyu Hong Kim [d], Vigor Yang [b]

[a] Pusan National University, Busan 46241, Republic of Korea
[b] Georgia Institute of Technology, Atlanta, GA 30332, USA
[c] Korea Aerospace Research Institute, Daejeon 34133, Republic of Korea
[d] Seoul National University, Seoul 08826, Republic of Korea

ARTICLE INFO

Keywords:
Supersonic combustion
Fuel temperature
Non-premixed combustion mode
Flame length
Convective Mach number
MLP (Multi-dimensional Limiting Process)

ABSTRACT

A comprehensive numerical study is undertaken to investigate the dynamics of hydrogen-air supersonic turbulent flames in a shear coaxial configuration. The effects of fuel temperature on the flow and flame characteristics are examined systematically. The numerical methodology is based on a hybrid RANS/LES model for compressible, multi-species flows with finite-rate chemical reactions. Results from simulations employing different levels of grid resolution and numerical schemes are compared and validated against experimental data. The importance of adequate grid resolution and high-order numerical schemes to achieve high-fidelity prediction of fine-scale flow features is underscored. In particular, the multi-dimensional high-order oMLP scheme shows remarkable prediction capabilities without incurring excessive computational cost. The lifted turbulent flame characteristics with combustion occurring mostly in a premixed mode downstream after turbulent mixing in the shear layer are identified and elaborated. A parametric study is subsequently performed to investigate the effect of fuel temperature. It is found that the combustion regime changes from partially-premixed to non-premixed mode as the fuel temperature is increased. The flame width and combustion efficiency increase with increasing fuel temperature, due to the enhancement of mixing following the reduced convective Mach number. The most prominent effect of fuel temperature is the reduction of flame length, a crucial factor for the design of supersonic combustors.

1. Introduction

In scramjet and rocket engines, turbulent combustion occurs under high-temperature, high-speed, and high Reynolds-number operating conditions. In liquid rocket engines, such as staged-combustion and expander-cycle engines [1–5], fuel is delivered to the main combustion chamber at a subsonic speed under supercritical pressures [6]. In scramjet engines, on the other hand, supersonic flows are sustained throughout the engine to avoid excessive heating and pressure losses while ensuring completion of combustion and energy release within a reasonable length. Although the scramjet design does not in itself impose constraints on injector fuel state, several engine configurations incorporate staged-combustion or expander cycles. For example, the X-51A demonstrator employed a regenerative cooling system [7], while the HyFly (Hypersonic Flight Demonstration) program uses a dual combustion ramjet (DCR) engine in which pre-burned fuel is delivered to the supersonic combustor [8].

Injection of high-temperature fuel can, in theory, greatly enhance the ignition and flame stabilization characteristics in a scramjet engine, but only limited research has been reported on such effect in the literature. More extensive investigation is warranted, especially considering the complex nature of flowfields involving shock-wave interactions and compressibility effects, coupled with turbulence and chemical kinetics. The key scientific question to be pursued is to what extent fuel temperature affects flow structures, flame characteristics, and combustion efficiency at realistic engine operating conditions. The present numerical work is intended to address this issue that would otherwise be formidable to pursue experimentally. A series of parametric studies is

* Corresponding author.
E-mail address: aerochoi@pusan.ac.kr (J.-Y. Choi).
[1] These authors contributed equally to this work.

https://doi.org/10.1016/j.fuel.2022.125310
Received 22 March 2022; Received in revised form 10 July 2022; Accepted 14 July 2022

Table 1
Numerical studies of hydrogen-air coaxial supersonic combustion. † PNS (Parabolized Navier-Stokes equations), RANS (Reynolds Averaged Navier-Stokes), LES (Large Eddy Simulation), DNS (Direct Numerical Simulation), ILES (Implicit LES), MILES (Monotone Integrated LES), EBU (Eddy Break-Up model), PDF (Probability Density Function), PSR (Perfectly Stirred Reactor), PaSR (Partially Stirred Reactor), MIL (Model Intermittent Lagrangian).

Reference	Configuration	2D*/ 3D	Turbulence modeling	Number of species	Kinetics mechanism	Combustion modeling
Evans and Schexnayder (1980) [36]	Evans [34]	2D	PNS	7 species	Spiegler [37]	EBU, laminar
Eklund et al., [38]	Evans [34], Cheng [35]	2D	RANS	7 species	Jachimowski [39]	laminar
Baurle et al., (1994) [40]	Cheng [35]	2D	RANS	7 species	Jachimowski [39]	PDF
Zheng and Bray (1994) [41]	Evans [34]	2D	RANS	Fast-chemistry	–	PDF flamesheet
Norris and Edwards (1997) [42]	Evans [34]	2D	LES	9 species	Balakrishnan [43]	laminar
Sabel'inkov et al., (1998) [44]	Evans [34]	2D	RANS	9 species	Balakrishnan [45]	CMC/PDF Flamelet
Gerlinger et al., (1998) [46]	Evans [34]	2D	RANS	7 species	Baurle [40]	laminar
Gerlinger et al., (2001) [47]	Evans [34]	2D	RANS	7 species	Baurle [40]	PDF
Möbus et al., (2001) [48]	Cheng [35]	2D	RANS	7 species	Baurle [40]	PDF
Möbus et al., (2003) [49]	Evans [34], Cheng [35]	2D	RANS	7 species	Baurle [40]	PDF
Baurle and Girimaji (2003) [50]	Cheng [35]	2D	RANS	7 species	Baurle [40]	PDF
Davidenko et al., (2003) [51]	LAERTE [52]	3D	RANS	7 species	Various [38,40,53]	laminar
Dauptain et al., (2005) [54]	Cheng [35]	3D	LES	4 species	Fit to Yetter [55]	laminar
George et al., (2006) [56]	LAERTE [57]	2D	LES	7 species	Eklund [38]	PSR, PaSR
Xiao et al., (2007) [26]	Cutler [58]	2D	RANS	7 species 9 species	Jachimowski [39] Conaire [59]	Variable Sc_t, Pr_t
Izard et al., (2009) [60]	Cheng [35]	2D	RANS	9 species -	Jachimowski [39]	MIL
Keistler and Hassan (2010) [61]	Cutler [58]	2D	RANS	7 species 9 species	Jachimowski [39] Conaire [59]	Variable Sc_t, Pr_t
Gerlinger et al., (2010) [62]	Cheng [35]	2D	RANS	4 ~ 9 species	Various [39,59,63–66]	PDF
Koo et al., (2011) [67]	Evans [34]	3D	LES	9 species	Mueller [53]	PDF
Donde et al., (2011) [68]	Evans [34]	3D	LES	9 species	Mueller [53]	PDF
Boivin et al., (2012) [69]	Cheng [35]	3D	LES	5 species	Boivin [70]	laminar
Gomet et al., (2012) [71]	Evans [34], Cheng [35]	2D	RANS	9 species	Jachimowski [39]	MIL
Karaca et al., (2012) [72]	LAERTE [57]	3D	LES	7 species	ONERA [73]	MILES
Lu et al., (2012) [74]	assumed	3D	DNS	9 species	Li [75]	laminar
Jin et al., (2013) [76]	assumed	3D	DNS	9 species	Li [75]	laminar
Luo et al., (2013) [77]	assumed	3D	DNS	9 species	Li [75]	laminar
Moule et al., (2014) [78]	Cheng [35]	3D	LES	9 species	Jachimowski [63]	U-PaSR
Ribert et al., (2014) [79]	Cheng [35]	3D	LES	5 species	Boivin [70]	laminar
Koo et al., (2015) [80]	assumed	3D	DNS	9 species	Mueller [53]	laminar
Zhang et al., (2015) [81]	Evans [34]	2D	LES	7 species	Singh [82]	laminar
Bouheraoua et al., (2017) [83]	Cheng [35]	3D	LES	5 species	Boivin [70]	laminar
Almeida et al., (2019) [84]	Cheng [35]	3D	LES	9 species	Yetter [55]	Flamelet/ PDF
Karaca et al., (2019) [85]	LAERTE [57]	3D	LES	7 species	ONERA [73]	ILES

*2D: two-dimensional simulation with axisymmetric assumption.

carried out to investigate the effect of fuel temperature in the range of 300–1500 K, covering practical fuel injection temperatures relevant for scramjet operation.

Various types of supersonic combustor configurations have been tested experimentally worldwide, and numerical studies for these configurations have also been carried out. Lin et al., [9] investigated experimentally a realistic scramjet engine configuration. Companion numerical studies were also reported [10,11]. Micka and Driscoll [12] performed experiments on a dual-mode combustor with a cavity flame holder. Koo et al., [13] numerically studied the dynamic characteristics of the same combustor using large eddy simulation. Fundamental characteristics of supersonic combustion have also been investigated using canonical configurations. A simple yet realistic configuration is transverse fuel injection into a supersonic crossflow, which was employed in the Hyshot-II flight test [14] and its ground experiment [15]. This configuration has been simulated numerically by several researchers [16–19]. Another configuration studied widely is supersonic combustor with a strut injector, where fuel is injected at the base of a strut [20]. Such a configuration was adopted in several numerical efforts to understand the flame structure and to develop accurate numerical models for supersonic combustion [21–24]. One canonical representation is combustion in a supersonic shear layer. Burrows and Kurkov [25] performed measurements for parallel wall jet injection in a supersonic combustor. Several numerical studies were conducted based on this setup for the evaluation of numerical methods and combustion models [26–29]. Another basic configuration is the shear coaxial supersonic injector with co-flowing air. The air is typically vitiated through combustion to generate a high enthalpy supersonic flow. The present study on the effect of fuel temperature on supersonic turbulent hydrogen-air flames is based on this configuration.

This paper is organized as follows. Section 2 provides a brief survey of various numerical studies on coaxial supersonic combustion. Section 3 describes the numerical modeling approach for the present study. The physical configuration and flow conditions are presented in Section 4. In Section 5 several numerical simulation issues are examined, including grid resolution, numerical schemes, and model validation for supersonic turbulent flames. Following the development and validation of the numerical approach, a series of simulations is conducted by varying the fuel temperature. The effects of fuel temperature on supersonic combustion characteristics are presented in Section 6.

2. Review of numerical studies on hydrogen/air coaxial supersonic turbulent combustion

Coaxial fuel injection with co-flowing air has been studied by many researchers to understand the fundamentals of turbulent non-premixed combustion and its lift-off flame characteristics under subsonic conditions [30–33]. There are very limited experimental studies for supersonic conditions in the public domain, however, due to difficulties associated with realizing supersonic flow conditions with reasonable flow enthalpy or temperature. Among the most widely studied experiments are those by Evans et al., [34] and Cheng et al., [35] conducted on hydrogen-air flames in supersonic coaxial flow configuration. A variety of numerical studies have been carried out for these configurations to develop numerical methods and combustion models, and to study the structure and characteristics of supersonic flames. Table 1 summarizes the numerical studies in the literature on hydrogen-air coaxial supersonic combustion, organized by publication year.

Supersonic combustion is highly turbulent, and is characterized by high-frequency fluctuations in flow variables, due to the high Reynolds numbers involved. Turbulent eddy motion has been found to govern the dynamic characteristics of supersonic combustion [86]. With advancements in computing capabilities, LES has become an attractive technique for predictive modeling of turbulent combustion [87], allowing resolution of eddy motion at scales where fuel–air mixing and combustion are relevant. One of the earliest LES studies on coaxial supersonic combustion was conducted by Norris and Edwards [42] using 2D axisymmetric LES and the laminar chemistry combustion model. In spite of the 2D assumption and omission of subgrid turbulence-chemistry interactions, the results agreed fairly well with measured data as the grid resolution was increased. This trend could be attributed to capturing the finer scales of eddy motion, and the consequent reduction in the error associated with the unresolved scales at higher grid resolution. Dauptain et al., [54] attempted 3D LES of Cheng's configuration with two-step kinetics and coarse mesh. Their results showed accurate prediction of not only mean flow quantities, but also the level of fluctuations with respect to the experimental values. George et al., [56] applied the PSR and PaSR combustion models to their 2D LES, and in their results both wall pressure distribution and ignition delay were estimated well. Koo et al., [67] developed an Eulerian PDF method called the direct quadrature method of moments (DQMOM), and coupled the method to compressible LES simulations. Donde et al., [68] further extended the DQMOM model to the semi-discrete quadrature method of moments (SeQMOM) method for better representation of the PDF. However, the results from Eulerian PDF methods seem to be similar in terms of accuracy to those obtained without any closure. Boivin et al., [69] carried out a fine-scale numerical simulation to validate their three-step reduced chemistry mechanism. The solution is obtained in a DNS-like approach using a compressible flow solver and the laminar chemistry model without subgrid scale closure of turbulence-chemistry interactions. It thus can be considered as an ILES approach. Karaca et al., [72] reported the results from LES of non-reacting and reacting jets using a 5th-order WENO scheme with and without explicit subgrid model (i.e., LES and ILES, respectively). Their results indicate that the Smagorinsky model is too dissipative. While the selective structure function model showed slightly better results, it did not prove to be superior to ILES. They also found that resolution is much more crucial than subgrid models to obtain closer agreement with experimental data. A subsequent study by Karaca et al., [85] demonstrated that ILES with a high resolution scheme is able to predict turbulent supersonic combustion, even without subgrid turbulence-chemistry closure, though this is not the case for subsonic combustion. Ribert et al., [79] carried out a fine scale LES study without closure, and later further studied the detailed structure and dynamics of the lifted jet flame using a very fine grid [83]. The grid resolution in their study is about five times the Kolmogorov scales and sufficient to resolve the flame, which is considered state-of-the-art resolution for a supersonic coaxial turbulent flame. Interestingly, they identified detonation-like features in turbulent non-premixed flames, due to shock-flame interactions [83]. Zhang et al., [81] used a similar LES framework without closure to study the flame dynamics of coflow ethylene and air with a splitter plate. Almeida and Martinez [84] applied a PDF model in an LES solver to study supersonic lifted flames, and found that subgrid contributions are important for coarse meshes and that the stochastic fields approach is capable of modeling those effects.

In addition to the RANS and LES studies described above, DNS studies have also been carried out for coaxial supersonic turbulent flames [74,76,77,80]. To achieve the required grid resolution, however, the Reynolds number was reduced significantly by reducing the length scale or the density of fuel and air, rendering the results unsuitable for comparison with experimental data.

3. Physical models and numerical methods

3.1. Axisymmetric 2D LES

A key finding from previous studies is that the accuracy of simulations is more dependent on the numerical resolution than the models. Typically, grid refinement studies are performed and a grid which is fine enough to produce a converged solution is used for further investigation. It is interesting to note that there is lack of similar efforts on the use of high-resolution numerical schemes to capture the fine scale flow features. Therefore, a comparative assessment of numerical schemes with different orders of accuracy is warranted and would be a topic of interest in conjunction with grid refinement study.

The physics of turbulent combustion in supersonic fuel and air jets, including the flow and flame features, have been investigated in LES studies [69,78,83,84]. Limited studies, however, have been undertaken to evaluate the parametric effect of flow variables on the mixing and combustion characteristics. This is primarily due to the fact that the computational cost of performing well-resolved 3D LES simulations is enormously high and prohibitive. A more affordable approach should be sought to undertake such parametric studies.

The use of a 2D model would be a natural choice for a tractable approach compared to full 3D simulations. The computational cost for a 2D simulation would be of the order of 1 % or less than that of a 3D simulation, since hundreds of grid points are typically used in each direction for 3D LES studies. A 2D model may not accurately capture the 3D vortex breakdown mechanisms leading to formation of small-scale structures by wrinkling along transverse direction causing increased mixing area. Therefore, 2D model may not be sufficient to account for small-scale mixing. However, they provide sufficient accuracy in capturing large-scale vortex rollup, mixing and shock trains which are important factors in the near-field flow and flame characteristics [42,81]. Although axisymmetric 2D simulation loses some features of realistic flow physics, the essential characteristics of flow structures and the cascade of energy transfer are still retained [88,89]. The 2D LES study by Norris and Edwards [42] showed fairly good agreement with the measurements of Evans et al., [34], and was able to capture the salient features of coaxial supersonic flames. Based on their findings, the present work employs 2D axisymmetric LES for efficient study over the large parameter space. The baseline simulation is validated against experimental case of Evans et al., [34].

3.2. Theoretical model

In this study, turbulence is treated using Menter's shear stress transport model, along with the detached eddy simulation (SST-DES) technique [90]. This formulation behaves as a LES closure to capture detailed eddy motions in the main separated and free-shear layers, while the model converges to the $k-\omega$ RANS model near surface boundaries to circumvent the high-resolution requirements of fine-scale wall turbulence. In other words, the formulation works as LES in the combustion regions and as RANS in the wall boundary layers inside the injector.

The Favre-filtered form of the conservation equations of mass, momentum, energy, and species concentration are solved numerically in a fully coupled manner, along with the transport equations for turbulent kinetic energy and vorticity. The set of equations is represented in a conservative form as follows:

$$\frac{\partial \mathbf{Q}}{\partial t}+\frac{\partial \mathbf{F}}{\partial x}+\frac{\partial \mathbf{G}}{\partial y}+\mathbf{H}=\frac{1}{Ra}\left(\frac{\partial \mathbf{F}_v}{\partial x}+\frac{\partial \mathbf{G}_v}{\partial y}+\mathbf{H}_v\right)+\mathbf{W} \tag{1}$$

$$\mathbf{Q}=\begin{bmatrix}\rho_j\\ \rho u\\ \rho v\\ \rho e\\ \rho k\\ \rho\omega\end{bmatrix},\ \mathbf{F}=\begin{bmatrix}\rho_j u\\ \rho u^2+p\\ \rho uv\\ \rho hu\\ \rho ku\\ \rho\omega u\end{bmatrix},\ \mathbf{G}=\begin{bmatrix}\rho_j v\\ \rho uv\\ \rho v^2+p\\ \rho hv\\ \rho kv\\ \rho\omega v\end{bmatrix},\ \mathbf{H}=\frac{1}{y}\begin{bmatrix}\rho_j v\\ \rho uv\\ \rho v^2\\ \rho hv\\ \rho kv\\ \rho\omega v\end{bmatrix} \tag{1a}$$

$$\mathbf{F}_v=\begin{bmatrix}-\rho_j u_j^d\\ \tau_{xx}\\ \tau_{xy}\\ \beta_x\\ \mu_k\frac{\partial k}{\partial x}\\ \mu_\omega\frac{\partial \omega}{\partial x}\end{bmatrix},\mathbf{G}_v=\begin{bmatrix}-\rho_j v_j^d\\ \tau_{xy}\\ \tau_{yy}\\ \beta_y\\ \mu_k\frac{\partial k}{\partial y}\\ \mu_\omega\frac{\partial \omega}{\partial y}\end{bmatrix},\mathbf{H}_v=\frac{1}{y}\begin{bmatrix}-\rho_j v_j^d\\ \tau_{xy}\\ \tau_{yy}\\ \beta_y\\ \mu_k\frac{\partial k}{\partial y}\\ \mu_\omega\frac{\partial \omega}{\partial y}\end{bmatrix},\mathbf{W}=\begin{bmatrix}w_j\\ 0\\ 0\\ 0\\ s_k\\ s_\omega\end{bmatrix} \tag{1b}$$

where $\mathbf{Q}$ is the conservative variable vector, $\mathbf{F}$ and $\mathbf{G}$ the convective flux vectors, $\mathbf{F}_v$ and $\mathbf{G}_v$ the diffusive flux vectors, $\mathbf{H}$ and $\mathbf{H}_v$ the axisymmetric terms, and $\mathbf{W}$ the vector of source terms containing the chemical reaction and turbulence model terms. All the flow variables are non-dimensionalized, and Ra is the Reynolds number based on the speed of sound and the inner injector diameter as the reference values. The ideal-gas law is used to calculate pressure from mixture density and temperature. Temperature is calculated implicitly from the total energy, which is defined as the sum of kinetic energy and internal energy. The internal energy and other thermodynamic properties of each species are calculated using the NASA polynomial fit based on the thermally perfect gas assumption. The laminar values of dynamic viscosity and thermal conductivity of each species are determined as a polynomial fit of temperature. Fick's law of mass diffusion is used to evaluate the diffusion velocity, in which binary mass diffusivity is obtained using the Chapman–Enskog theory in conjunction with the Lennard–Jones intermolecular potential functions. The viscosity and thermal conductivity of the mixture are calculated using Wilke's mixing rule. The mathematical and numerical procedures for handling the coupled equations are documented in the authors' previous works [16,91,92].

A major issue in turbulent combustion modeling lies in the selection of turbulent Prandtl and Schmidt numbers. A turbulent Prandtl number of 0.9 or 1.0 has been widely accepted and used in most numerical studies of supersonic combustion. On the other hand, a variety of turbulent Schmidt numbers in the range of 0.4–1.0 were employed in the works listed in Table 1. In the present study, the turbulent Prandtl and Schmidt numbers are set to be 0.9 and 0.5 respectively, following the numerical study of Baurle and Edwards [93].

Chemical kinetics are another point of complexity. A variety of detailed mechanisms have been developed for hydrogen combustion, and some of them have been used for coaxial supersonic combustion, as listed in Table 1. The authors' group has compared the accuracy of a number of mechanisms in predicting ignition delay and flame speed, as well as shock induced combustion [94]. A seven-step hydrogen–oxygen reduced mechanism based on Jachimowski's detailed mechanism [39] is employed in this study, for computational efficiency. The model includes six reacting species ($O, O_2, H, H_2, OH,$ and H_2O), and nitrogen (N_2) as inert species. Reaction species and reaction steps are identical to the abridged version used by Baurle [40], but reaction parameters from the original detailed mechanism [39] are retained since the validation of reaction data for ignition delay and flame speed is more clearly shown in the original paper. Reactions involving HO_2 and H_2O_2 are neglected in this reduced mechanism, since they are only relevant for low-temperature ignition. Since the static temperature of the air flow entering the scramjet combustor is of the order 1000 K or above, the low temperature reactions can be neglected here. This is well justified in the present study, which focuses on the effect of fuel heating. Berglund et al., [95] showed in their LES studies on supersonic turbulent combustion that the high-temperature combustion mechanism is superior to the one-step and two-step mechanisms.

LES of a turbulent reacting flow requires closure of unresolved reaction terms to account for turbulence-chemistry interactions at the subgrid scale. A number of PDF-based turbulence closures have been developed for RANS studies of supersonic combustion, and further extended for LES applications [46–50,67]. Agreement with experimental data was reasonable, although not significantly different from the results with the laminar chemistry model. A thorough comparison of several closure models for turbulent combustion was conducted by Fureby [96,97]. These models can be expressed as a scaling of the reaction rate computed from the laminar chemistry model [18,98,99], and the results with more sophisticated closure models exhibit little to no difference when compared with the results using the laminar chemistry model [27,67]. The laminar chemistry model is, therefore, widely used in many studies, as noted in Table 1. Karaca et al., [72] postulated that the unresolved species flux is balanced by the difference between the real reaction rates and those evaluated from the quasi-laminar formula for LES of compressible reacting flows. They also showed that simulation accuracy is more dependent on numerical resolution than on the subgrid model. The present work employs the laminar chemistry model and focuses on the importance of numerical resolution, rather than subgrid turbulent-chemistry interactions.

3.3. Numerical schemes

There have been limited evaluations of the role of accuracy and resolution of various numerical methods in simulations of supersonic turbulent combustion. A comparative assessment of numerical schemes with different orders of accuracy is undertaken in the present work in conjunction with a grid refinement study. The first goal of the present work is to establish accurate and robust numerical methods for simulating supersonic turbulent combustion. Since fuel–air mixing and reactions occur at small length and time scales, the numerical scheme must be able to capture fine-scale eddy motions. In supersonic flows, the intrinsic hyperbolic characteristics trigger numerical instabilities in discontinuous regions, such as shock waves. This hinders the use of high-order central-difference schemes. Upwind discretization schemes, known as flux splitting schemes, are essential for numerically stable computation of supersonic flows. Flux splitting schemes are, however, first order accurate in general. It is necessary to extend to higher order accuracy while preserving monotonicity at the discontinuity.

Monotonicity-preserving high-resolution schemes such as Monotonic Upstream-Centered Scheme for Conservation Laws (MUSCL) [100] or Weighted Essentially Non-Oscillatory (WENO) [101] schemes are commonly used to achieve high-order accuracy in continuous flow regions, with a first order accuracy in discontinuous regions. These schemes were, however, originally developed based on one-dimensional analysis of the scalar convection equation, and inevitably have accuracy and stability issues in multidimensional problems. Kim and Kim [102] developed a multi-dimensional limiting process (MLP) scheme to eliminate numerical oscillation and ensure stable and monotonic calculation of a multi-dimensional discontinuity. The MLP scheme has been applied in limited studies of turbulent combustion [103], scramjet and rocket combustion [104,105]. It has also been extended to the optimized MLP (oMLP) scheme, which classifies continuous and discontinuous regions based on Gibbs phenomena [106]. The high-order scheme is applied for continuous regions, and MLP for discontinuous regions. The overall approach has been demonstrated for aero-acoustics problems [106]. In this study, the fifth-order oMLP scheme (oMLP5) [106] is implemented and its performance is compared with third-order MUSCL (MUSCL3) [107] and fifth-order WENO (WENO5) schemes [108].

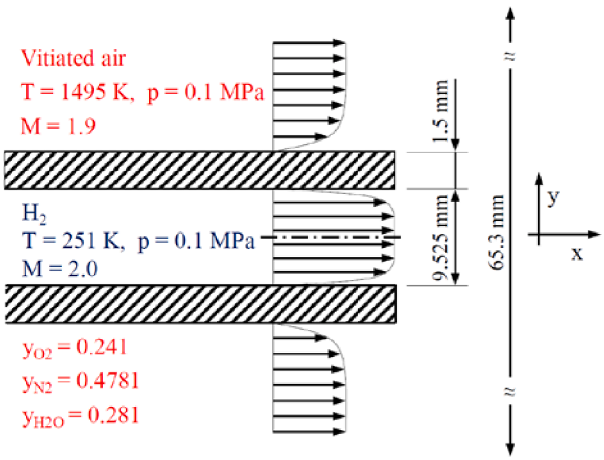

Fig. 1. Flow conditions and configuration of experimental Case 1 of Evans et al., [34].

The governing equations and associated boundary conditions are solved in a fully coupled manner using a fully implicit approach. The computational framework used for the present study is incorporated in an in-house code that has several types of flux splitting schemes combined with high resolution schemes. The code has been developed, validated, and applied for a variety of problems [16,29,81,86,91,92,107,109]. The AUSMPW + flux splitting scheme [110] is used in the present study, since it showed the least numerical dissipation in the previous studies when used in combination with the high-resolution schemes. Viscous fluxes are discretized by a fourth-order central-difference scheme. Second-order implicit time integration is used with maximum four sub-iterations to get time-accurate results [107]. The code is parallelized with the OpenMP technique to optimize the performance in machines with multi-core shared-memory processors (SMP).

4. System configuration and flow conditions

The experimental configuration identified as Case 1 by Evans et al., [34] is adopted as the baseline in the present work. This setup has been numerically investigated by many researchers using both RANS and LES methods [42,67,68], although there is some disagreement among reported results due to the lack of detailed information about the original experimental configuration. Fig. 1 shows a schematic of the configuration [34] with flow conditions for the hydrogen fuel and vitiated air. The incoming air is heated and vitiated by burning a small amount of hydrogen. The injector is assumed to be straight, to account for the boundary layer effect at the injector lip. Ambient air is ignored for simplicity, and the interface between the vitiated air and the ambient air is emulated by a slip wall boundary condition. RANS result for the reference condition with the ambient air shows that the effects on the fuel/air mixing later is quite limited. This simplification has been used in other studies [47,67] as well. Supersonic outflow boundary conditions are applied at the outlet. The wall surfaces are modeled with a no-slip, adiabatic wall boundary condition. The inlet boundary conditions are described in Fig. 1. A uniform inflow velocity profile is applied, and a boundary layer is allowed to develop naturally as the flow passes over the splitter plate. The flow Reynolds number is calculated as 5.08×10^4 for the air stream based on the outer diameter of the fuel injector, and 1.81×10^5 for the fuel stream based on the inner diameter. The Kolmogorov length scales are estimated as $l_\kappa = l_0/Re^{\frac{3}{4}}$, where l_κ, l_0 are the Kolmogorov and integral length scales, respectively. The inner and outer diameters of the injector are taken as the integral scales for the fuel and oxidizer streams respectively to obtain *a priori* estimates for grid resolution requirements. The corresponding Kolmogorov length scale estimates at the injector lip are 0.74 μm and 2.81 μm, respectively.

A three-block grid system is constructed for the configuration in Fig. 1, comprising the fuel injector, air nozzle and main combustor. The total length of the computational domain is 52.4 cm. Four levels of grid resolution are considered for a grid convergence test. The grid points in the main combustor are 241 × 51, 481 × 101, 961 × 201, and 1,921 × 401, respectively. As an example, Fig. 2 shows the coarsest grid, which has 241 × 51, 25 × 31, and 25 × 16 points in the main combustor, air nozzle, and fuel injector, respectively. Among the 241 grid points in the axial direction of the main combustor, 201 points are uniformly distributed from the injector lip to the location of $x/d_j = 26.2$, up to where experimental measurements are available. The remaining 40 points are allocated in the extended region, which is made radially divergent to keep the supersonic outflow away from any downstream disturbances. Grid points are clustered toward the solid surface to capture boundary-layer effects and the near-field mixing. The transverse grid spacing is moderately relaxed in the downstream region while maintaining sufficient resolution in the core of the mixing layer to adequately capture the mean flow and flame structures. The same clustering factors are maintained for all of the grid levels. The number of grid elements in the nozzle and injector are increased by a factor of 2 in each direction between subsequent levels of resolution. Table 2 summarizes the grid resolution levels used for the grid refinement study. The y^+ values calculated based on the wall shear stress are as follows. For the fuel injector, $\Delta y^+ = 1$ corresponds to a near-wall grid spacing of $\Delta y = 9.98\mu m$ and $y^+ = 5$ is $y = 49.9\mu m$. For the air injector, $\Delta y^+ = 1$ is $27.8\mu m$ and $y^+ = 5$ is $139.3\mu m$. Comparing the grid resolutions in Table 2, the Level 1 grid includes only one grid point within the viscous sublayer ($y^+ < 5$) and is not fine enough to resolve the viscous sublayer on the fuel side. For the Level 4 grid, two or three grid points are included within the viscous sublayer on the fuel side and the minimum grid spacing is even smaller than $\Delta y^+ = 1$ on the air side. The resolution of the Level 3 and Level 4 grids are considered to be sufficient for hybrid RANS/LES, since the minimum grid resolution is just one order of

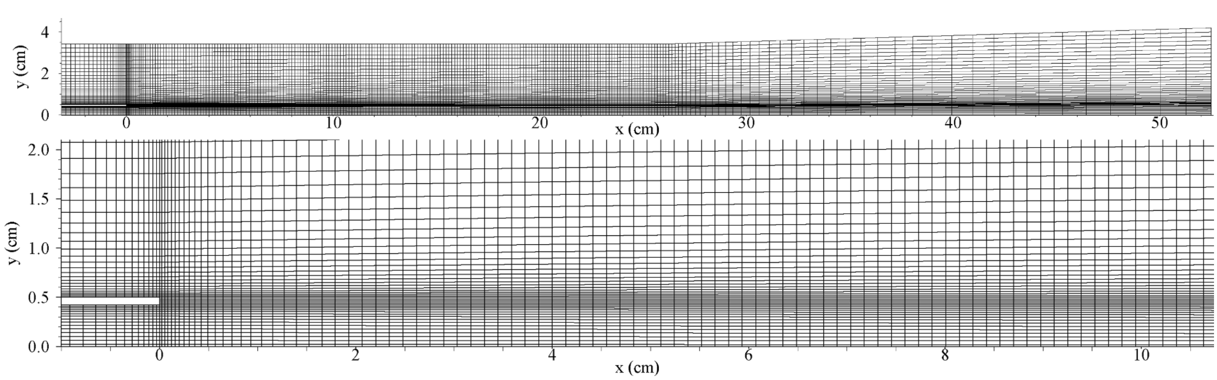

Fig. 2. Computational domain with the smallest grid (241 × 51). Full view (top), near-injector view (bottom).

Table 2
Grid resolution and minimum grid spacing for each block at different resolution levels.

	Fuel Stream		Air Stream		Combustor	
	no. of grid points	Δy_{min} (μm)	no. of grid points	Δy_{min} (μm)	no. of grid points	Δy_{min} (μm) fuel/air
Level 1	25 × 16	119.9	25 × 31	150.0	241 × 51	150.0 / 235.2
Level 2	49 × 31	58.8	49 × 61	63.7	481 × 101	74.5 / 116.0
Level 3	97 × 61	29.2	97 × 121	30.5	961 × 201	37.2 / 57.5
Level 4	193 × 121	14.5	193 × 241	15.0	1,921 × 401	18.6 / 28.7

magnitude higher than the Kolmogorov scale at the injector lip. In the present study, the RANS model is active only in the near-wall region of the injector to model the boundary layer development, while the flow physics in the main combustor region, which is the primary region of interest, is essentially modeled using LES. The Kolmogorov scales increase as the flow moves downstream along the shear layer, but the grid resolution is maintained at the same level to the end of the computational domain.

The transverse grid resolution for the Level 2 grid is around 75–100 μm, while for the Level 4 grid it is around 15–30 μm near the centerline of the splitter plate and less than 50 μm near the centerline of the combustor (bottom boundary). This is well within the range of resolutions typically employed for resolving the flame in past studies. For example Boivin et al., [69] use mesh resolutions of 100–400 μm, Moule et al., [78] use a resolution of 200 μm, and the study of Bouheraoua et al., [83] considered the finest grid resolution of 60 μm. The grid resolutions considered in this study are therefore considered suitable to resolve the flame thickness with sufficient resolution.

5. Grid resolution study

Simulations were carried out for the baseline case at the conditions shown in Fig. 1 using the four levels of grid resolution described above. Time integration is performed using an implicit scheme with sub-iterations within each time step. The stability and accuracy of the present scheme has been thoroughly studied for unsteady combustion phenomena [92,107]. The scheme is shown to be stable and accurate for CFL numbers nominally greater than 1.0. It is also shown that four sub-iterations is sufficient to maintain the temporal accuracy. In the present study the time integration is conducted with CFL number of 1.0 with four sub-iterations for numerical stability over wide range of conditions. A total of 500,000 time steps is performed for each case. The physical time step and total time duration were 66.0 ns and 32.98 ms for the Level 1 grid, and 7.48 ns and 3.74 ms for the Level 4 grid, respectively. The initial 100,000 time steps were computed to reach a quasi-steady state. Thereafter, time averaging of the flow variables was performed for the remaining 400,000 time steps. The flow through time (FTT) is estimated as 0.347 ms, based on the domain length and velocity of the air stream. For the Level 4 grid, the initial transient time to reach a quasi-steady state was 0.748 ms (~2.15 FTTs), and the time period for statistical averaging was 2.99 ms (~8.62 FTTs), which is considered sufficient to obtain statistically converged flow properties.

Fig. 3 shows the instantaneous and time-averaged distribution of the magnitude of density gradient as predicted by the Level 4 grid using different numerical schemes. Kelvin-Helmholtz (KH) instabilities appear in the early phase of the shear layer and prompt fuel/air mixing and

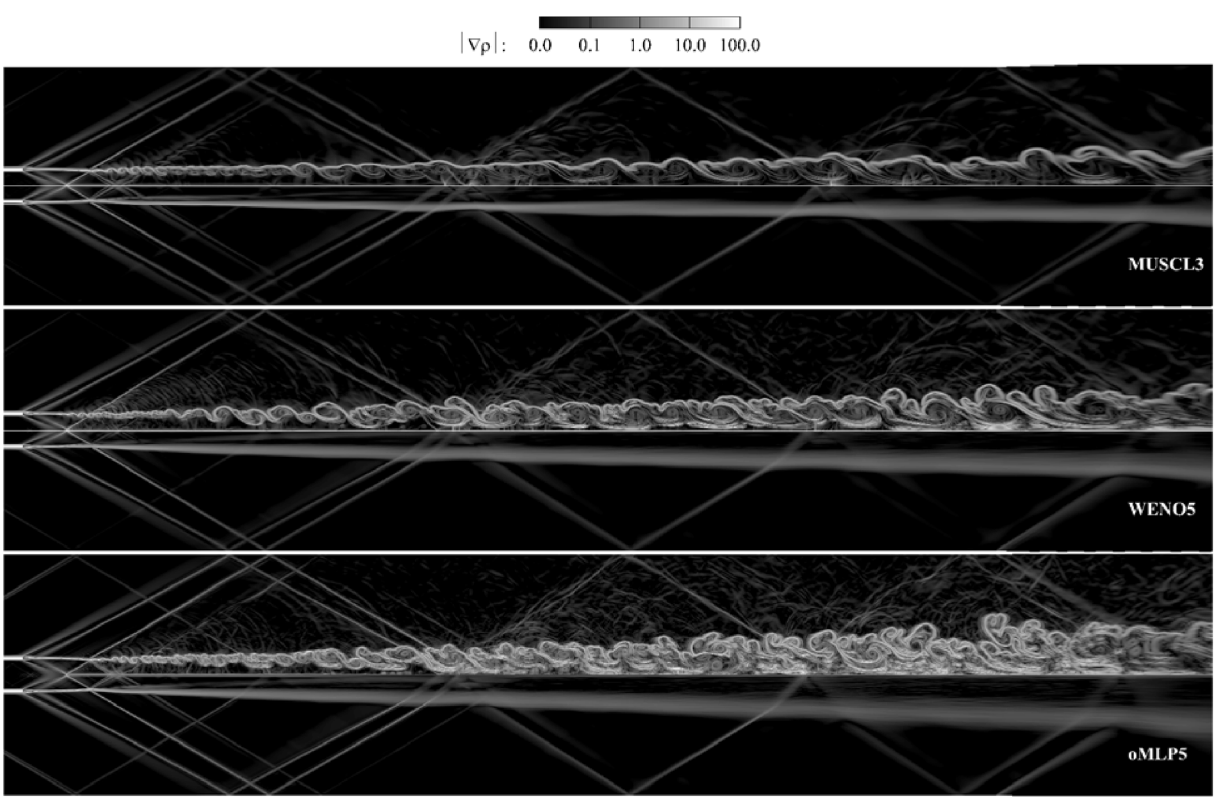

Fig. 3. Instantaneous (top half) and time-averaged (bottom half) density gradient magnitude distributions: various numerical schemes, Level 4 grid.

reaction. They develop further downstream and transition to turbulence. It is clear that each numerical scheme has a different ability to resolve eddy motion. The WENO5 scheme captures acoustic and vortical structures with better definition than the MUSCL3 scheme, and the strength of eddies is also preserved further downstream. The oMLP5 scheme resolves the fine-scale eddy structures most distinctively, which is critical for accurate prediction of turbulent mixing and combustion. The MLP scheme used in this study has been systematically validated for several different cases, including turbulent combustion [103–105] and aero-acoustic problems [106]. The scheme has been shown to yield strict monotonicity-preserving and dispersion-relation preserving properties in addition to high accuracy over an extended range of wavenumbers. The increased range of flow structures captured are a direct consequence of the extended-wavenumber accuracy of the scheme, rather than unphysical oscillations which are inherently damped out. Kim et al., [106] report a suite of rigorous test cases often encountered in acoustic/shock wave problem showing strict accuracy criteria that are met by the MLP scheme. Gerlinger [103] also shows the usefulness of MLP scheme for turbulent flow simulation.

The time-averaged results reveal that the predicted shear layer thickens and widens as the numerical scheme moves from MUSCL3 to WENO5 to oMLP5. Since the supersonic shear layer is formed between two streams of different Mach numbers, weak shock and expansion waves appear at the injector tip and reflect at the computational boundary. The interaction of the reflected waves with the turbulent shear layer is considered not to be strong enough to change the overall characteristics. Nonetheless, inclusion of a computational domain for the ambient air or an accurate boundary condition to avoid such artificial interactions should be considered in future work.

Fig. 4 and Fig. 5 show the calculated profiles of time-averaged pitot pressure and water vapor mass fraction, respectively, compared with experimental data. The predicted width of the shear layer grows as the grid resolution and the numerical scheme become more refined. The time-averaged shear-layer thickness depends on the resolved eddy motion. As the grid resolution or numerical scheme is refined, finer scale flow features are resolved. This includes small scale vortices, flow instabilities and their interactions with the shock waves, and small-scale species gradients. The mixing behavior resulting from these features are adequately accounted for and this directly results in increased mixing predicted on finer grids, resulting in a thicker shear layer on average. The results of MUSCL3 with a 1,921 × 401 grid are closer to those of WENO5 with a 481 × 101 grid. This implies that the fifth-order WENO5 scheme provides accuracy comparable to that of the third-order MUSCL3 scheme with a 4-times coarser resolution (i.e. 16 times fewer grid elements in 2D). The results of oMLP5 with a 481 × 101 grid are between the WENO5 results with the 961 × 201 and 1,921 × 401 grids, which means that the accuracy of the WENO5 scheme with one-dimensional interpolation can be achieved with the oMLP5 scheme using multi-dimensional interpolation with half the spatial resolution (i.e. 4 times fewer grid elements in 2D).

A drawback of the axisymmetric assumption is also observed here. The numerical results agree well with experimental data in the outer region, but show some deviation in the core. This is because the zero-flux condition imposed at the axis of symmetry prevents the transport of mass, momentum, and energy. As a result, and unlike the experimental results, sharp gradients of flow variables appear in the flow field close to the axisymmetric boundary. Regardless of this deviation at the centerline, the flow field in the outer mixing layer is predicted quite well and the numerical results converge to the experimental data when finer grids and better numerical schemes are used. There is also a noticeable deviation between the simulation and experimental data observed around $r/d_j \sim 0.45$, for the 481x101 grid and MUSCL3 cases. This region corresponds to the mixing layer interface between the fuel and oxidizer. The deviation can be attributed to insufficient resolution across the injector lip. The error is decreased and results match progressively better with experimental data for the cases with increasing grid resolution and

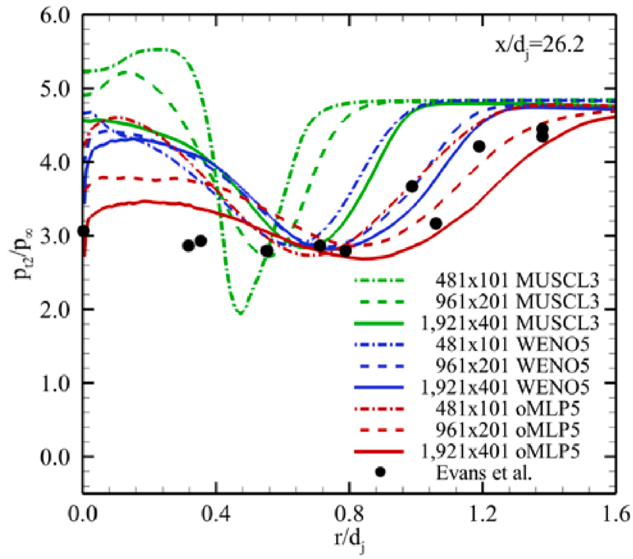

Fig. 4. Pitot pressure distribution from different numerical cases compared with experimental data.

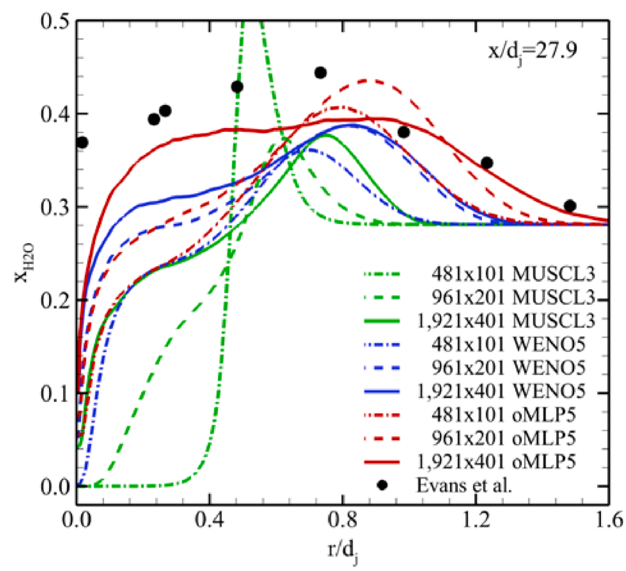

Fig. 5. H_2O mole fraction distribution from different numerical cases compared with experimental data.

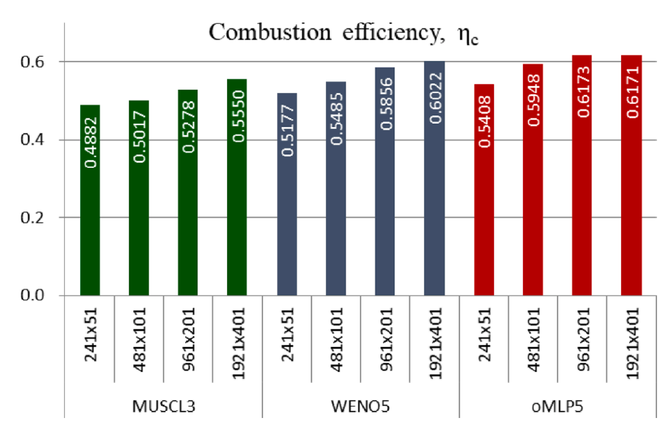

Fig. 6. Combustion efficiencies at the combustor exit for all numerical cases.

Table 3
Computational time per iteration using Dell EMC R640 with dual Intel® Xeon® Gold 6154 (18 cores, 3.00 GHz) processor.

Grid level	No. of grid points	Computing time/iteration (ms)		
		MUSCL3	WENO5	oMLP5
Level 1	241 × 51	15.91	16.18	22.70
Level 2	481 × 101	48.56	50.96	59.78
Level 3	961 × 201	215.70	220.31	218.75
Level 4	1,921 × 401	1,251.88	1,281.19	1,287.50

using better numerical schemes. The results obtained from the Level 4 grid with oMLP5 scheme are closest to the experimental data.

As a measure of numerical convergence, a simple but comprehensive parameter would be appropriate to evaluate overall convergence characteristics or performance. In this regard, combustion efficiency is considered. The combustion efficiency is a measure of the degree of completion of combustion and is also used to quantify heat addition in experiments. In this study, combustion efficiency calculated using Eq. (2) is used to assess numerical convergence and combustor performance.

$$\eta_c = 1 - \frac{\left(\int_o^R y_{H_2}\rho u dy\right)_{x=exit}}{\left(\int_o^R y_{H_2}\rho u dy\right)_{x=inlet}} \tag{2}$$

Fig. 6 summarizes the combustion efficiency at the exit of the computational domain for the different cases. For the MUSCL3 scheme, combustion efficiency increases as the grid becomes finer and does not converge within the grid resolutions considered. The WENO5 scheme shows a higher value than the MUSCL3, but with no substantial improvement in the convergence behavior. As the grid resolution is refined, finer scale flow features are resolved, including small scale vortices, flow instabilities and their interactions with the shock waves, in addition to small-scale species gradients. The mixing behavior of these interactions are adequately accounted for, and this directly results in increased mixing predicted on finer grids. For the oMLP5 scheme, the combustion efficiencies estimated with the 961 × 201 and 1,921 × 401 grids are very similar. These values are interpreted to be the converged combustion efficiency that can be obtained with the present flow conditions and physical models.

Another important factor to consider in numerical simulations is the computational cost incurred with high-order numerical schemes. Table 3 indicates the computational time for one time step for each case, as evaluated on a Dell EMC R640 with dual Intel® Xeon® Gold 6154 (18 cores, 3.0 GHz) processor used for the simulations. The computational cost increases by a factor of 3 to 6 with the increase in grid resolution. However, it is interesting to note that the increase in computational cost from MUSCL3 to WENO5 to oMLP5 is marginal, especially at higher grid levels. This factor, combined with the grid resolution required to achieve the same level of accuracy, as discussed previously, is an important consideration for high-fidelity and efficient numerical simulation.

Given the results of the various comparisons made here, we use the 1,921 × 401 grid with the oMLP5 scheme to investigate supersonic turbulent flame characteristics for the rest of the paper.

6. Structure of supersonic turbulent flame for the baseline condition

The supersonic turbulent flame structure is investigated using two parameters, the scalar dissipation rate (SDR,$\chi \equiv 2D\nabla^2 f$) and Takeno's flame index $\left(\mathrm{FI} \equiv \frac{\nabla y_{fuel}\bullet\nabla y_{ox}}{|\nabla y_{fuel}||\nabla y_{ox}|}\right)$, both of which have been widely used in analyses of turbulent non-premixed combustion [111,112]. Here, f is the mixture fraction, defined as.

$$f = y_H + y_{H_2} + y_{OH}\frac{M_H}{M_{OH}} + y_{H_2O}\frac{M_{H_2}}{M_{H_2O}} \tag{3}$$

where y_j and M_j are the mass fraction and molecular weight of species j. Moderate SDR levels are necessary to initiate and sustain non-premixed flames, although high SDR may lead to flame quenching. A positive FI represents premixed combustion mode, and a negative FI represents non-premixed combustion mode. The reaction pathway goes through a zone of high concentration of transition species, such as OH, before combustion is completed with the final product H_2O. Thus, a higher OH mass fraction corresponds to actively reacting regions of the flame, while a higher H_2O mass fraction indicates regions where the reaction is nearly complete.

Fig. 7 shows instantaneous and time-averaged distributions of the OH mass fraction y_{OH}, SDR, and FI. The OH concentration is relatively low at the beginning and becomes more prominent downstream. The basic characteristics of the supersonic turbulent jet flame are similar to that of a subsonic turbulent lifted flame. The variation of SDR is highest across the fuel–air interface; this variation is stronger at the beginning of the mixing layer and gradually decreases as the shear layer widens in the downstream part of the jet plume. FI is predominantly negative in the near-field of the injector but becomes mostly positive downstream. Correlating the regions of higher OH mass fraction with the distributions of the other two combustion parameters, it is found that the combustion primarily occurs in the moderate SDR ($1 < \chi < 10$) and positive FI regions. Only a small amount of OH is observed in some regions with high SDR and negative FI, indicating lower intensity of reactions.

Fig. 8 shows the radial distributions of the three reaction parameters at four different axial locations. The flame region is identified by the red band, where the peak of the OH mass fraction is located. In the near field at $x/d_j = 6.56$,y_{OH} has a peak value of 0.9 × 10^{-3} where FI is mostly negative, and SDR is about 4.2. At $x/d_j = 13.8$,y_{OH} has a peak value around 1.33 × 10^{-3}, while FI varies from negative to positive and SDR is between 2.0 and 3.0. At $x/d_j = 20.0$, y_{OH} has a peak value close to 1.6 × 10^{-3}, while FI varies from positive (in the core) to negative (outer regions) and SDR is about 1.8. At $x/d_j = 26.2$, y_{OH} has a peak value close to 2.1 × 10^{-3}, while SDR is about 1.1 in this location. However, at this location, the OH distribution is spread over a wide region where FI is always positive. Overall, the peak values of SDR decrease within the flame region and FI becomes predominantly positive as we move downstream along the jet. These results suggest that supersonic combustion in this case occurs mainly in premixed mode after the early phase of fuel/air mixing, similar to a lifted flame in a subsonic jet. The magnitude of SDR in the reaction zone has the same order of magnitude as that observed in typical non-premixed flames.

Unlike in subsonic lifted flames [111], here the outer part of the jet ignites before the inner part, because of mixing with the high-temperature surrounding air. This flame branch could also act as an ignition source for combustion downstream, although the local air temperature is sufficiently high to promote auto-ignition. The asynchronous ignition of the inner and outer portions of the jet is also demonstrated in the small amount of OH mass fraction in the early phase. A limitation with the Takeno flame index is that it only distinguished between purely premixed and non-premixed flame regions and cannot be used to identify auto-ignition fronts distinctly. Other recently proposed flame markers such as chemical explosive mode analysis (CEMA) [113] or gradient-free identification methods [114,115] may be able to tackle these issues. The heat release rate is another indicator to locate and quantify the flame characteristics. Fig. 9 shows scatter plot distributions of the non-dimensionalized heat release rate (HRR) with respect to mixture ratio, colored by SDR and FI. The HRR increases with

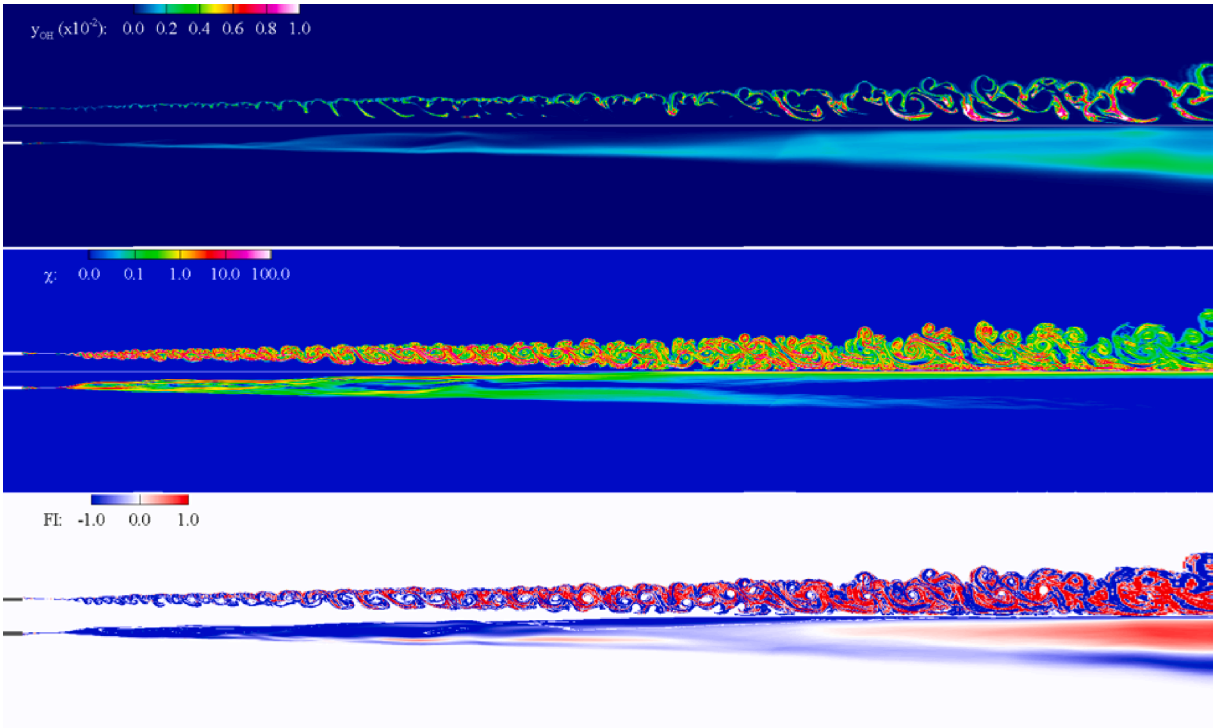

Fig. 7. Instantaneous (top) and time-averaged (bottom) combustion parameters.

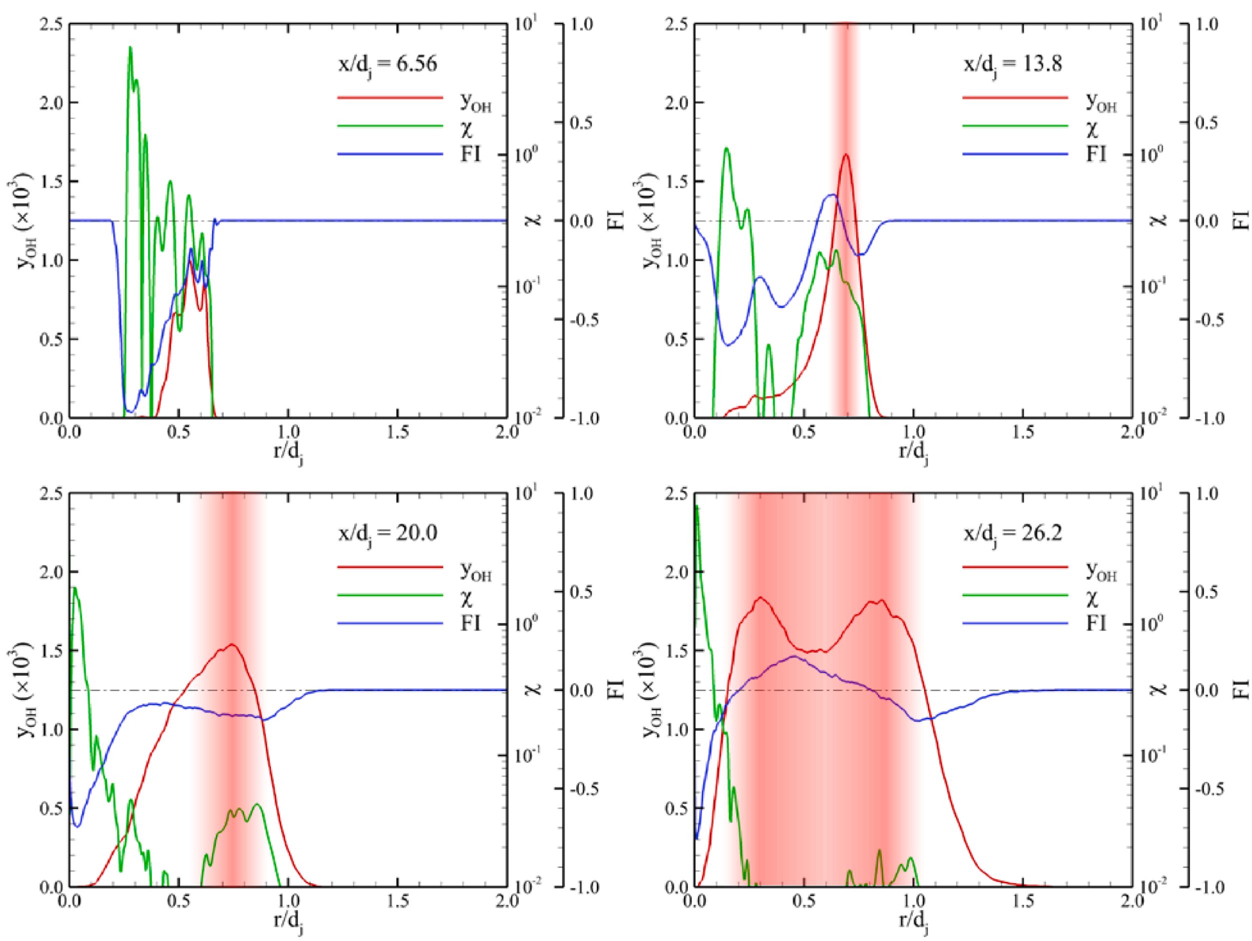

Fig. 8. Time-averaged reaction parameters at four axial locations.

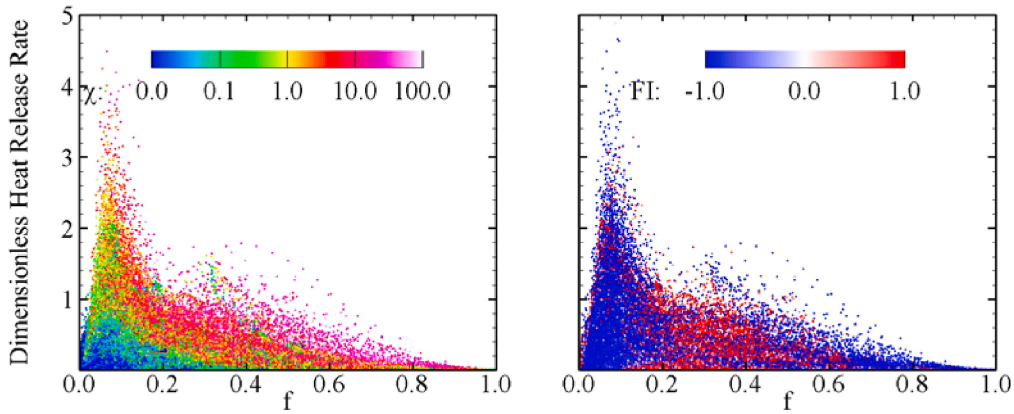

Fig. 9. Scatter plot of non-dimensionalized heat release rate vs mixture fraction colored by SDR (left) and FI (right).

increasing SDR, with peak values of the HRR occurring in the intermediate SDR (1–10 s^{-1}) regions. At higher SDR values, the non-premixed flame cannot be sustained due to depletion of radicals through diffusion. The flame zone, identified by the large HRR values, is distributed across both negative and positive ranges of FI, implying that combustion occurs in both non-premixed and premixed modes.

7. Effect of fuel temperature on flame characteristics

7.1. Conditions of parametric study

A parametric study was carried out to investigate the effect of fuel temperature on the combustion and flame characteristics. The physical configuration, computational setup, and numerical schemes remain the same as those used for the baseline study in Section 6. The fuel temperature was increased from 300 to 1,500 K in increments of 100 K. The maximum temperature of 1,500 K is high for regenerative cooling engines but could be considered as an upper limit for fuel-rich staged combustion cycle engines.

It should be noted that other flow properties are affected by changes in temperature, so additional constraints are necessary for the purpose of comparison. In the present study, a constant mass flow rate is enforced, with fixed density and flow speed corresponding to the experimental condition. As a result, fuel injection pressure increases linearly with fuel temperature, and fuel Mach number decreases from the reference condition. The variations of flow properties listed in Table 4 and plotted in Fig. 10. The speed of sound increases from 1,210 m/s at the experimental condition of 251 K to 2,959 m/s at 1,500 K. The increase in the speed of sound results in a decrease of fuel Mach number from 2.0 at 251 K to a subsonic value of 0.82 at 1,500 K. Since the Mach number is changed drastically, the effect of compressibility on fuel/air mixing should also be considered. To quantify the compressibility effect, the convective Mach number and compressibility function are calculated using Eqs. (4) and (5), following the definition by Papamoschou [116], and they are included in Table 4. The flow speeds of both fuel and air are fixed, and the convective Mach number changes from 0.455 to 0.243 due to the change in the speed of sound of the fuel.

$$M_c = \frac{|U_{H2} - U_{air}|}{a_{H2} + a_{air}} \tag{4}$$

$$f(M_c) = 0.25 + 0.75e^{-3M_c^2} \tag{5}$$

Table 4
Fuel properties as a function of inflow temperature.

T(K)	p_{H2}(MPa)	M_{H2}	M_c	$f(M_c)$
Baseline: 251	0.100	2.00	0.455	0.653
300	0.120	1.83	0.430	0.680
600	0.239	1.29	0.342	0.778
900	0.359	1.06	0.295	0.827
1,200	0.478	0.91	0.265	0.858
1,500	0.598	0.82	0.243	0.878

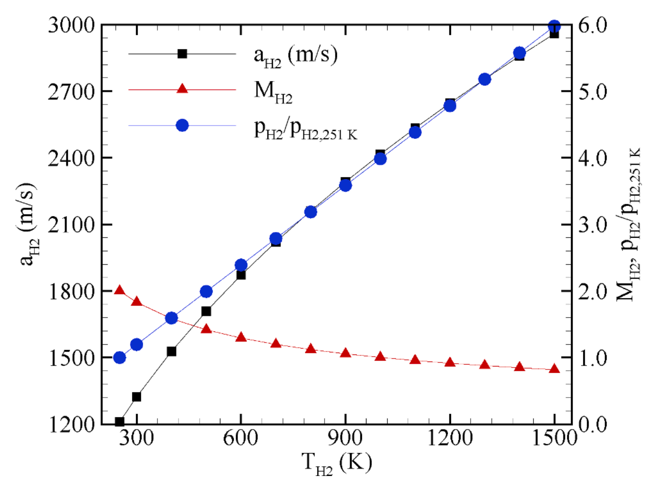

Fig. 10. Variation of fuel inflow properties.

7.2. Flowfield characteristics

Fig. 11 shows the instantaneous local Mach number and magnitude of density gradient for selected cases, and Fig. 12 shows the corresponding time-averaged distributions. For the reference experimental condition at 251 K, the fuel injection pressure is equal to the ambient air pressure of 0.1 MPa, corresponding to the situation of ideal expansion with no pressure difference between the two streams. The difference of Mach number between the fuel and air streams is limited to 0.1. Therefore, compressibility effects are very limited, and only a weak expansion wave exists at the injector lip caused by the finite thickness of the injector. As the fuel temperature increases, the fuel injection pressure increases, and the nozzle flow changes from perfectly expanded to

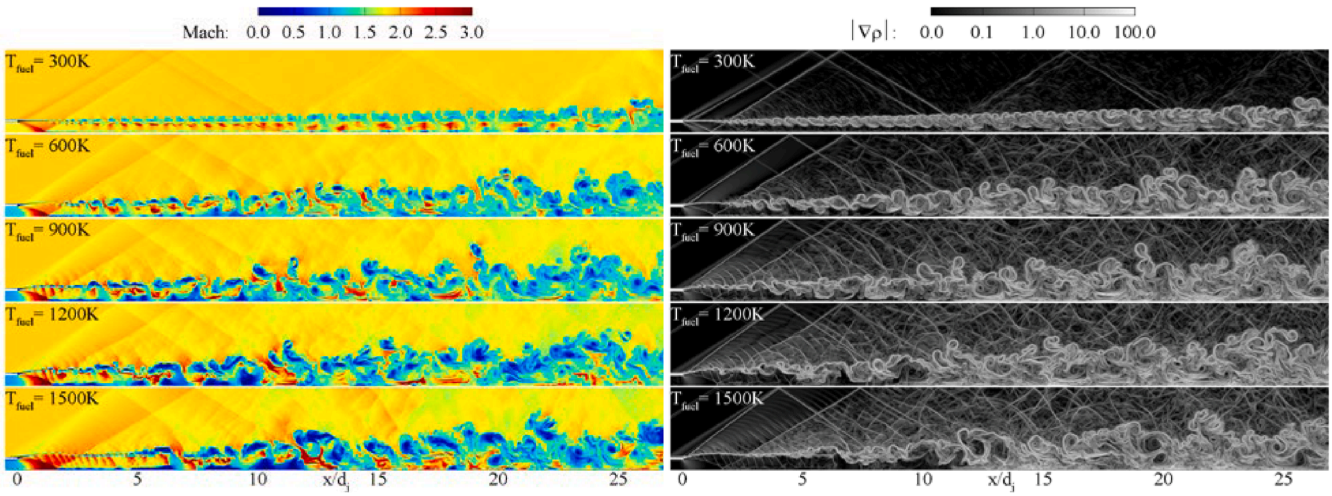

Fig. 11. Instantaneous local Mach number (left) and density gradient magnitude (right) distributions.

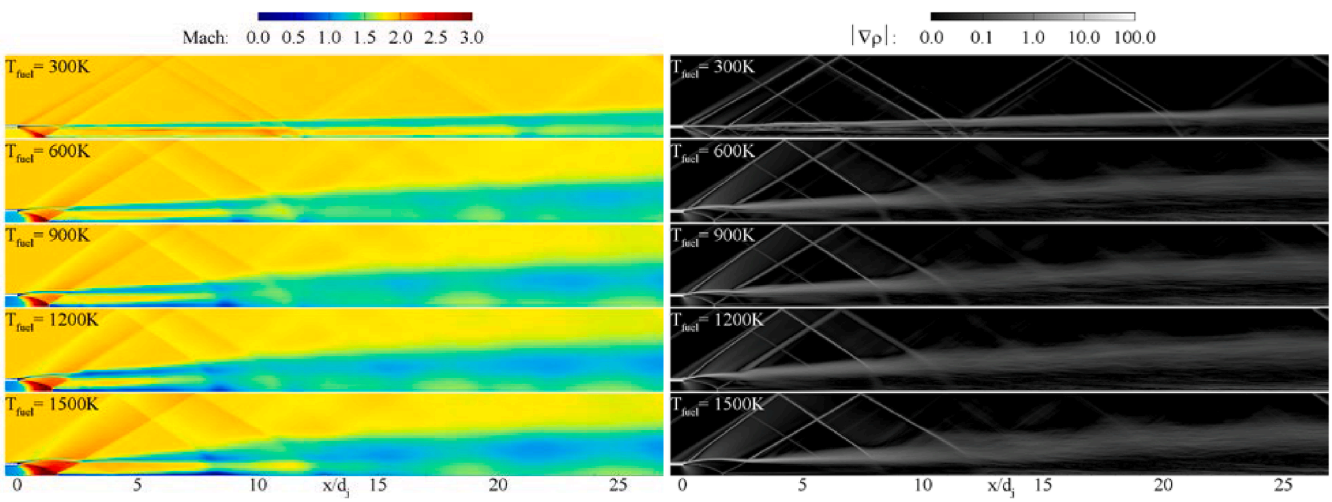

Fig. 12. Time-averaged local Mach number (left) and density gradient magnitude (right) distributions.

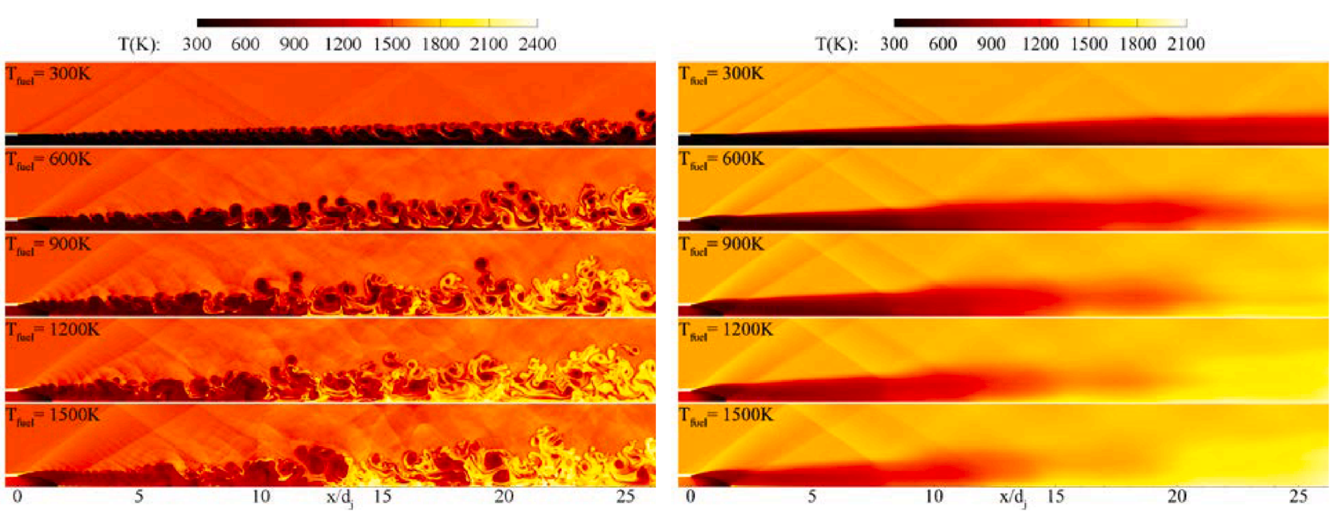

Fig. 13. Instantaneous (left) and time-averaged (right) temperature distributions.

under-expanded. Although the fuel injection Mach number decreases as the fuel temperature increases, the Mach number increases locally as the flow exits the injector due to external expansion. The convective Mach number and local Reynolds number are reduced with increasing fuel temperature. The decrease of convective Mach number results in larger vortical structures in the shear layer, as seen in Fig. 11, leading to enhanced shear-layer growth rate. This trend agrees well with previous investigations on compressible shear layers [116].

The large vortical structures interact with the incoming supersonic air stream, generating several Mach waves, as shown in Fig. 11. The density gradient plots reveal the presence of strong acoustic interactions that are generated at the jet exit. Owing to the expansion of the fuel stream at the injector exit, the fuel/air shear layer develops at an angle with respect to the incoming air flow, thereby inducing an oblique shock at the injector lip on the air side. The oblique shock reflects at the top wall boundary, and the reflected wave further interacts with the shear layer. This kind of shock-wave/shear-layer interaction plays a significant role in making the flowfield more turbulent, facilitating fuel/air mixing and combustion. Furthermore, as the pressure difference between the fuel and air streams increases with fuel temperature, the resulting shock wave and subsequent shock/shear layer interactions become stronger. The increase in pressure difference further widens the under-expanded fuel jet plume, leading to larger incident and reflected shock angles, and the shock-wave/shear-layer interaction regions become more closely spaced. This causes the flame stabilization to move closer to the injector tip.

7.3. Effect of fuel temperature on flame structure

In accordance with the change in flowfield characteristics, the flame structure is altered with fuel temperature. Fig. 13 presents instantaneous and time-averaged temperature distributions for representative cases. Combustion occurs within the large vortical structures where fuel and air mix. With increasing fuel temperature, the flame moves upstream toward the injector lip. Enhancement of combustion is easily identified by the overall increase in temperature within the domain. The length of the flame becomes shorter, and flame width increases.

Fig. 14 presents the instantaneous vorticity magnitude and OH mass fraction distributions in the near field region for the different cases. For the low fuel temperature case, the vortical structures in the near field are relatively smaller in size, resulting in weak entrainment and mixing of fuel and oxidizer streams. The OH mass fraction magnitudes are also low in the near field, implying that most of the combustion occurs in the downstream region after sufficient premixing is achieved. As the fuel temperature is increased, the coherent vortical structures are enlarged in size, leading to increased entrainment. Regions with high OH mass fractions are observed closer to the injector lip, suggesting that the combustion occurs closer to the injector in diffusion mode at higher fuel temperatures. The recirculation and mixing provided by these vortical structures initiate a premixed flame branch, which in turn provides a stabilization mechanism for the diffusion flame. These trends will be investigated in further detail in Section 7.4.

The combustion characteristics are more clearly understood from instantaneous and time averaged distributions of other variables. Fig. 15 and Fig. 16 show OH and H_2O mass fraction distributions, respectively. Mixture fraction and scalar dissipation rate (SDR,χ) are plotted in Figs. 17 and 18. The flame liftoff distance decreases as temperature increases, and the flame anchors to the injector lip at higher temperatures. The most active combustion zone, denoted by higher concentrations of OH mass fraction, shifts upstream closer to the injector.

In the high temperature cases, the flame shows a distinct transition at around$x/d_j = 10$, where an interaction between the reflected shock and mixing layer occurs. Even though the reflected shock from the top boundary is weak and does not have a strong effect on the flame in the baseline case, its strength increases with the fuel temperature. This effect contributes to combustion enhancement and flame stabilization. The effects of oblique shock waves have also been observed in the experimental work by Huh and Driscoll [117], where oblique shocks were induced using wedges. Fig. 17 shows that the distribution of mixture fraction is long and stretched for low fuel temperatures and becomes shorter and wider at high temperatures. Fig. 18 shows that in the early stage of the shear layer, the SDR is quite high where combustion is hard to sustain. The SDR is drastically reduced downstream of the shear layer, where most of the combustion is observed to occur. The interaction between the shock wave and mixing layer seems to reduce the magnitude of SDR, further facilitating combustion. As the fuel temperature increases, the SDR remains low over a wider region, and this prevents flame quenching and enhances combustion efficiency. Interestingly, the effect of fuel temperature on the SDR and other combustion parameters is manifested mainly up to 900 K, and the distributions are almost similar above 900 K. The decrease of convective Mach number in the fuel temperature range 900–1,500 K is lesser compared to decrease in the range 300–900 K. The compressibility function also starts to level off beyond 900 K. Because of the weak dependence of convective Mach number at higher temperature, the sensitivity of fuel temperature upon the growth rate of structures and flame characteristics is also relatively reduced.

Fig. 19 displays instantaneous and time-averaged flame index (FI) distributions. The blue and red regions are intermixed over the entire flame region for the entire fuel temperature range. In other words, premixed and non-premixed regimes of combustion co-exist, though there are some differences between the cases, as seen clearly in the two sets of plots. As the fuel temperature increases, the combustion regime changes from partially premixed to non-premixed dominant mode. Comparing the plots of FI, SDR, and mass fractions of OH and H_2O, the premixed regions exist primarily in the upstream and outer regions of the mixing layer, while combustion in other regions, including the combustor core, exhibit non-premixed characteristics. Overall, the combustion is predominantly held in non-premixed mode and this trend is intensified with increase in fuel temperature.

These findings support simplified flamelet-based modeling of the combustion. Non-premixed combustion models, solving both mixture fraction and reaction progress variable with reaction rate, are necessary for low temperature conditions, but a steady flamelet model, solving only mixture fraction and assuming fast chemistry, would be adequate for high temperature conditions.

The change of combustion characteristics from a combined premixed and non-premixed flame at low fuel temperatures to a non-premixed dominant flame at high temperatures is further illustrated by scatter plots of non-dimensionalized HRR distributions shown in Fig. 20. The plots are colored by scalar dissipation rate (SDR,χ) and flame index (FI). These can be contrasted with the reference case results in Fig. 9. The overall and peak HRR levels increase with increasing fuel temperature. As expected, higher HRR zones correlate with intermediate SDR ($1 < \chi < 10$) conditions, and the flame index plots show mixed patterns of positive and negative regions. It is interesting to note that at higher fuel temperatures, the bands of intermediate SDR become larger and the corresponding values of HRR are also higher. As the fuel temperature increases, the peak HRR regions (in the mixture fraction range $0 < f_{mix} < 0.2$) transition from mixed red-blue distributions to predominantly blue distribution. There are some red zones with lower HRR found in the higher mixture fraction (fuel-rich) regions. These zones correspond to the upstream premixed flame branch that stabilizes the non-premixed flame. The scatter plots support the previous discussion regarding combustion intensification and the change of combustion mode from partially premixed to non-premixed.

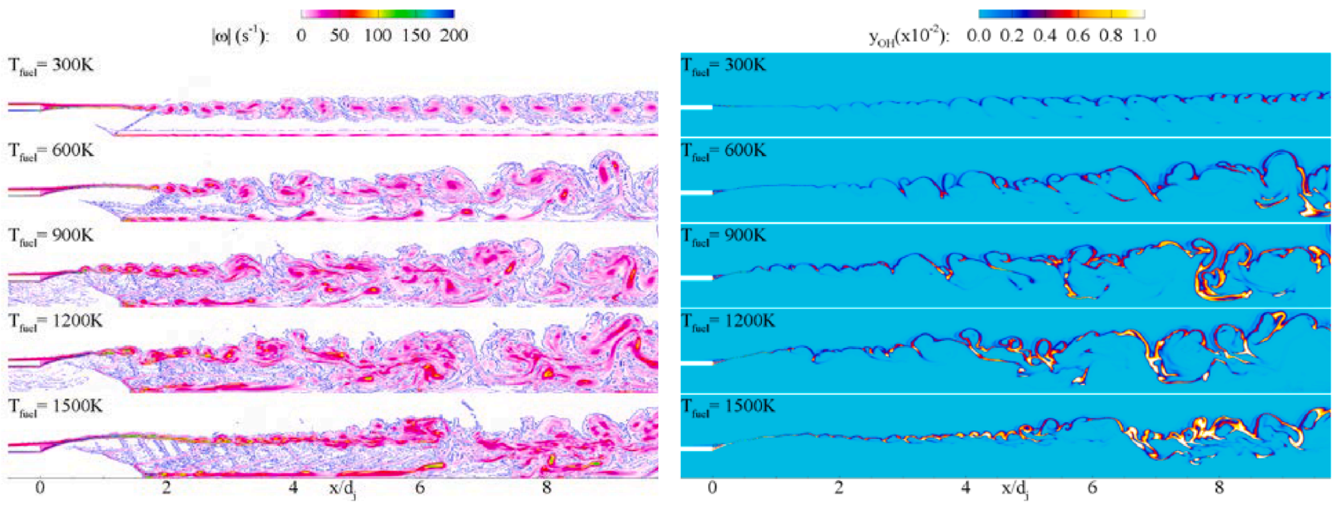

Fig. 14. Near-field distributions of instantaneous vorticity magnitude (left) and OH mass fraction (right).

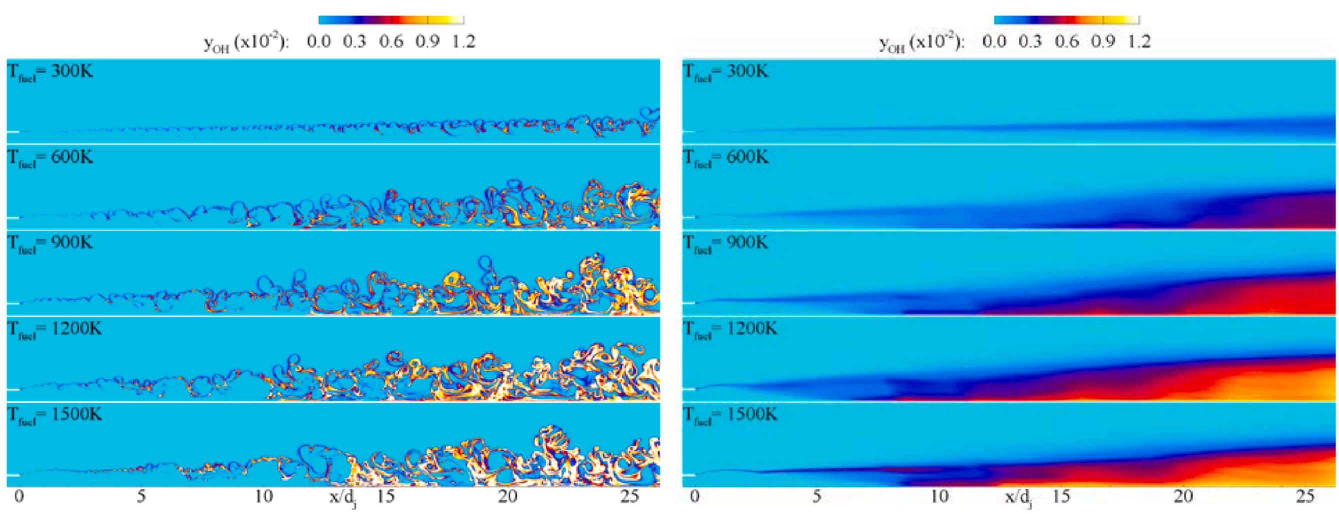

Fig. 15. Instantaneous (left) and time-averaged (right) OH mass fraction distributions.

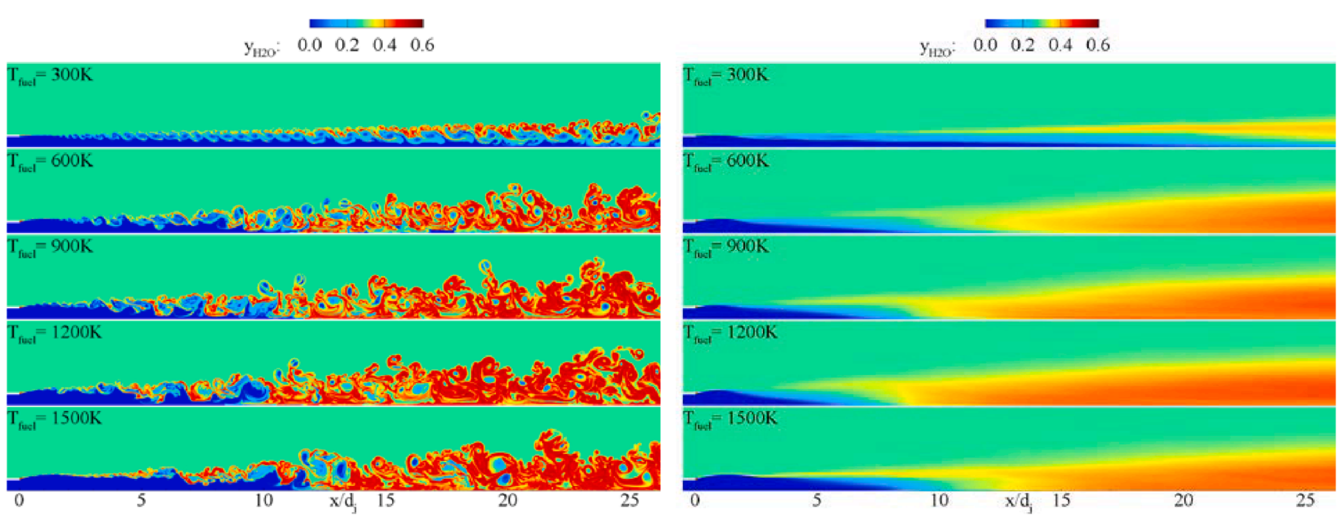

Fig. 16. Instantaneous (left) and time-averaged (right) H_2O mass fraction distributions.

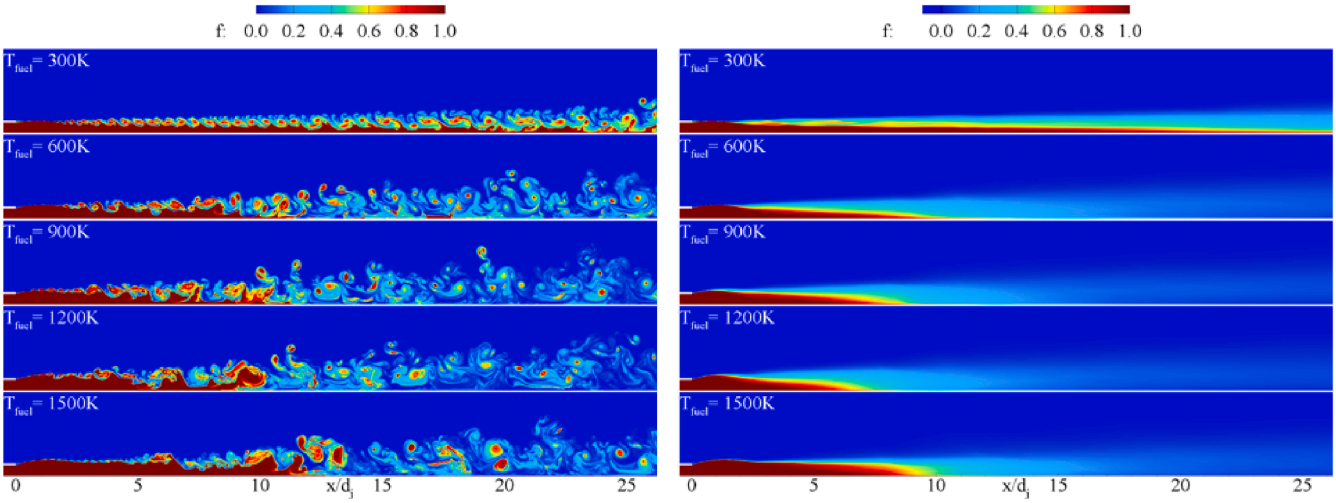

Fig. 17. Instantaneous (left) and time-averaged (right) mixture fraction distributions.

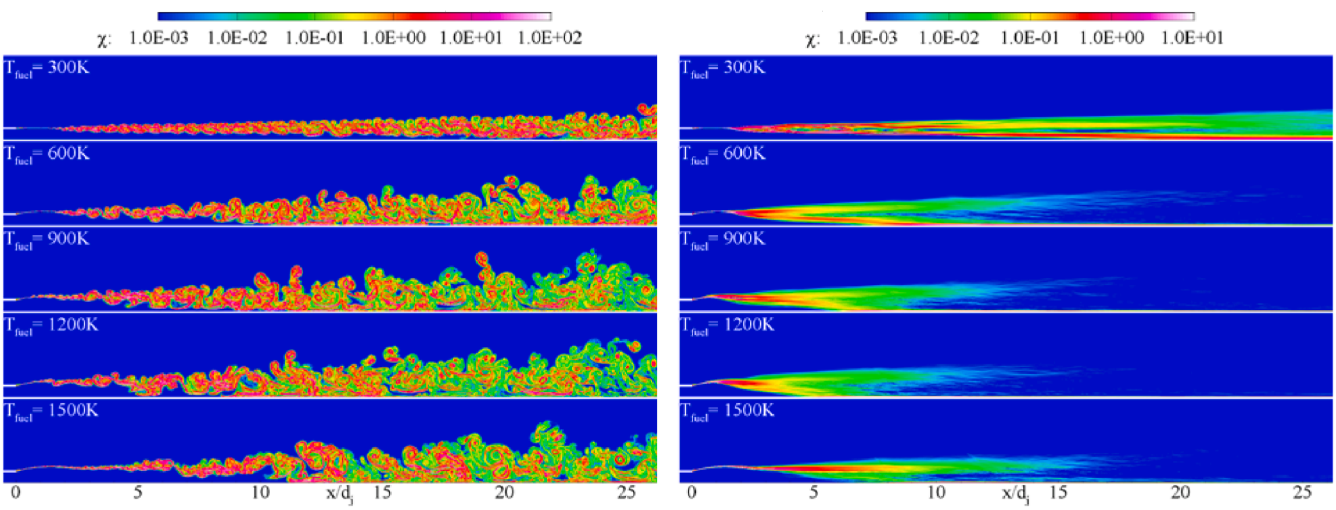

Fig. 18. Instantaneous (left) and time-averaged (right) scalar dissipation rate distributions.

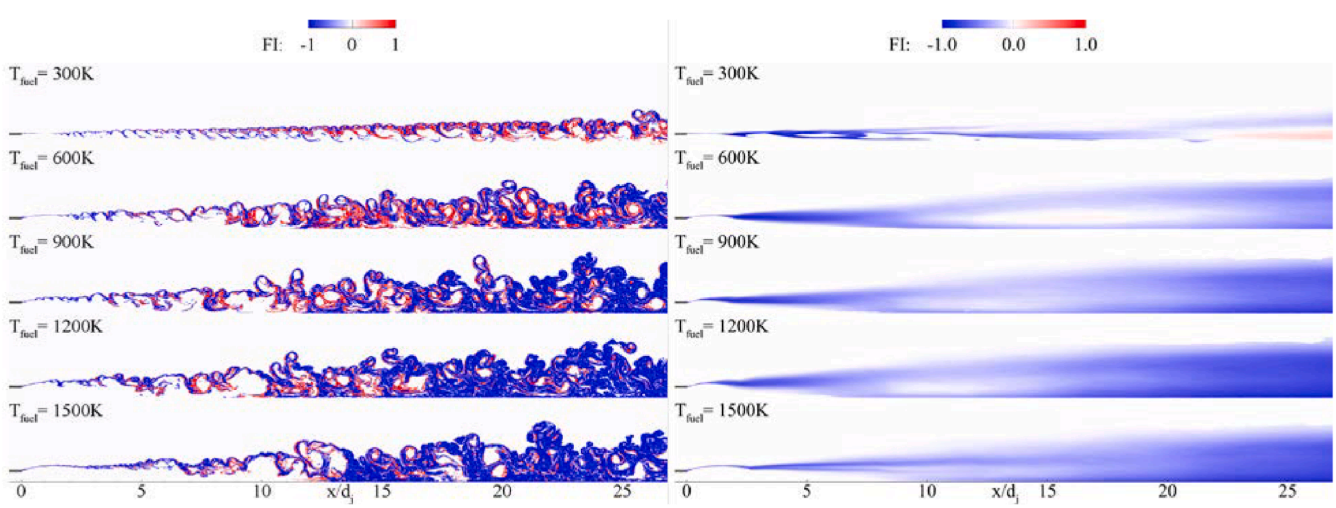

Fig. 19. Instantaneous (left) and time-averaged (right) flame index (FI) distributions.

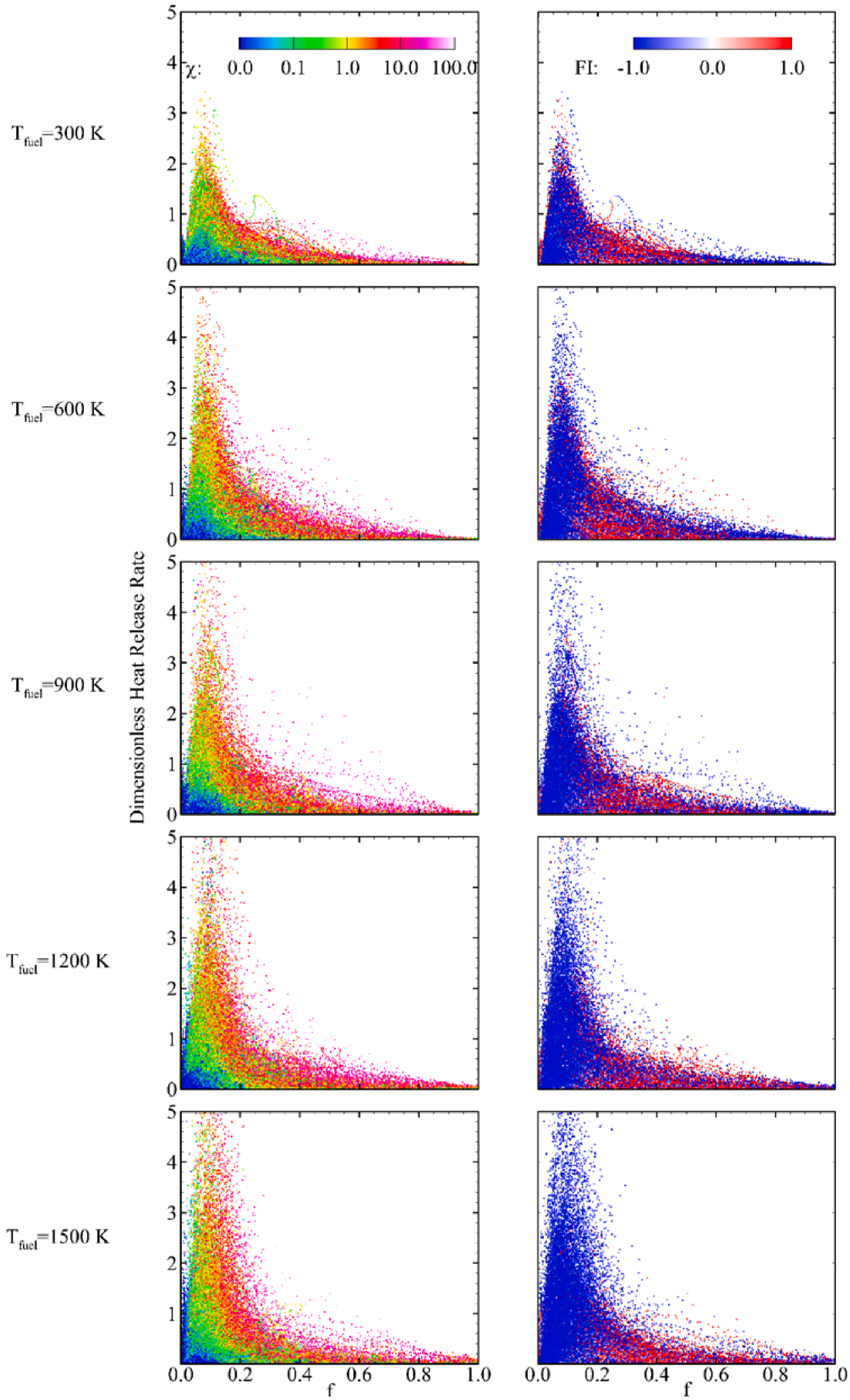

Fig. 20. Scatter plots of OH mass fraction as a function of the mixture fraction colored by (left) scalar dissipation rate (SDR, χ) and (right) flame index (FI) for selected cases at various fuel temperatures.

7.4. Effect of fuel temperature on overall combustion characteristics

Based on the local flowfield and flame structures discussed in the previous sections, the dependency of overall combustion characteristics, including flame length, width, and combustion efficiency, on the fuel temperature is investigated. The flame width and length are calculated from the time-averaged flame contours of the different cases. The flame contour is defined in general as the isoline of the stoichiometric mixture fraction. The stoichiometric mixture fraction is calculated to be 0.05973 for the mixture of fuel and vitiated air, but the ideal flame contour corresponding to this value is very long and extends out of the computational domain for the reference and low fuel temperature cases. Therefore, the flame contour for the current study is taken to be the isoline of mixture fraction value of 0.7, which corresponds to the mixture fraction at the exit of the centerline for the reference case. This definition of the flame contour is closer to the core of the fuel jet as compared to the ideal flame contour but is adopted for reasonable comparison between the different cases. The flame length and width are measured as the maximum length and width of the flame contour.

Fig. 21 presents the flame length and width measured from the time-averaged results at different fuel injection temperatures. The flame width increases initially with fuel temperature, and levels off around 600–900 K. It increases again at high temperature conditions due to external gas-dynamics expansion of the high-pressure fuel. The flame length, on the other hand, decreases rapidly as the fuel temperature increases and approaches a converged value at high temperatures. To further investigate the role of compressibility effects, the convective Mach number and the compressibility function from Table 4 are also plotted in Fig. 21. It is interesting to note that the variation of flame width is almost identical to that of the compressibility function. This is attributed to the fact that the growth rate of the mixing layer is determined by the compressibility function [116]. The flame width of the supersonic jet is mostly governed by the growth rate of the compressible mixing layer, which in this case is affected by the fuel temperature. However, it seems that the fuel temperature plays a more significant role in reducing the flame length under low temperature conditions. At high fuel temperatures, where non-premixed combustion is prominent, the flame length decreases more slowly as the convective Mach number decreases. In contrast, at low fuel temperatures, where mixed-mode combustion occurs, the flame length decreases drastically with increasing fuel temperature, possibly due to the additional chemical kinetic effect of the increase in laminar premixed flame speed. There appears to be an outlier for the flame length variation at T = 1,200 K as also seen in Fig. 17. This anomaly could be a system-specific operating condition triggering some form of shock-shear layer interactions and increased unsteadiness resulting in a mixing behavior that is larger than the neighboring cases. Another possible reason for this could be a numerical artefact stemming from a combination of modeling errors and incorrect time-averaging. The reduction of flame length with increased fuel temperature is of crucial significance for the design of supersonic combustors.

The combustion efficiency, calculated using Eq. (2), is plotted as a function of fuel temperature in Fig. 22. Fig. 22 shows that complete combustion is not attained for any of the cases in this study, perhaps because of the limited length of the computational domain. As discussed earlier, even the isoline of the stoichiometric mixture fraction is not fully contained within the computational domain. This means that a longer combustor is necessary for complete combustion under these conditions. The combustion efficiency increases with fuel temperature, partly due to enhanced mixing resulting from the decrease of convective Mach number, which is indirectly caused by increase of fuel temperature. The increased molecular diffusivities and reaction rates due to increased temperature also play a role in increasing mixing and combustion efficiency.

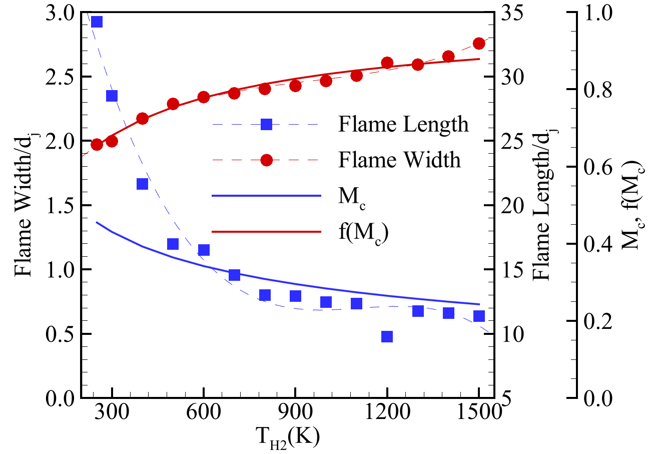

Fig. 21. Flame length and width for various fuel temperatures.

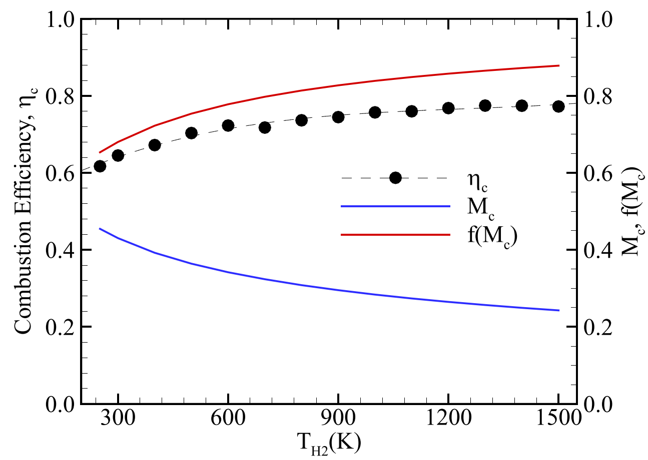

Fig. 22. Combustion efficiency for various fuel temperatures.

8. Conclusion

Numerical simulations of supersonic shear-coaxial turbulent flames were carried out to understand the effect of fuel temperature on flame structure and combustion characteristics. Numerical schemes with different orders of accuracy were investigated at different grid resolutions. Comparison of the numerical results with experimental data reiterates the importance of grid resolution, and particularly of high-resolution schemes for high-fidelity simulations. The multi-dimensional high-order oMLP5 numerical scheme resolves more fine-scale structures of the turbulent flowfield than the other schemes of consideration, and is shown to be more effective for reliable prediction of experimental results. The oMLP5 scheme also shows the best convergence behavior with relatively similar computational resource requirements.

The results for the baseline case reveal a lifted turbulent flame in which combustion is held mostly in a premixed mode in the downstream region after turbulent mixing in the shear layer. With increase in fuel temperature, the combustion regime switches from partially-premixed to predominantly non-premixed mode. The flame width and combustion efficiency increase as the fuel temperature increases. These trends are considered to be a result of mixing enhancement due to reduced convective Mach number at higher fuel temperatures. An important effect of fuel temperature lies in reducing the flame length and increasing combustion efficiency, which are crucial factors for the design of supersonic combustors.

Declaration of Competing Interest

The authors declare that they have no known competing financial interests or personal relationships that could have appeared to influence the work reported in this paper.

Data availability

No data was used for the research described in the article.

Acknowledgments

This research was supported by the Basic Research Program (No. 08-201-501-014) of the Agency for Defense Development of the Republic of Korea and the Senior Research Grant (NRF-2019R1A2C1004505) through the National Research Foundation (NRF) of Korea funded by the Ministry of Science and ICT (MSIT) of the Republic of Korea Government.

Appendix

A. Behavior of the SST-DES model and variation of turbulent viscosity

In the present study, the SST-DES model of Menter [90] is used. This model formulation involves a blending function and works as a LES subgrid scale model outside of the boundary layer and converges to a RANS k-ω SST model in the near-wall region of the boundary layer. This model is well-known in the DES turbulence modeling community and further details can be found in the original paper [90]. The RANS model is active only in the near-wall region of the injector to model the boundary layer development. The flow physics in the main combustor region, which is primary region of interest, is essentially modeled using LES. Fig. 23 shows the distribution of the ratio of turbulent viscosity μ_{turb} as computed from the SST-DES model to the total viscosity $\mu_{tot}(=\mu_{lam}+\mu_{turb})$. Although the turbulent viscosity diminishes outside the boundary layer, its value and contribution still remain finite within the core of the mixing layer.

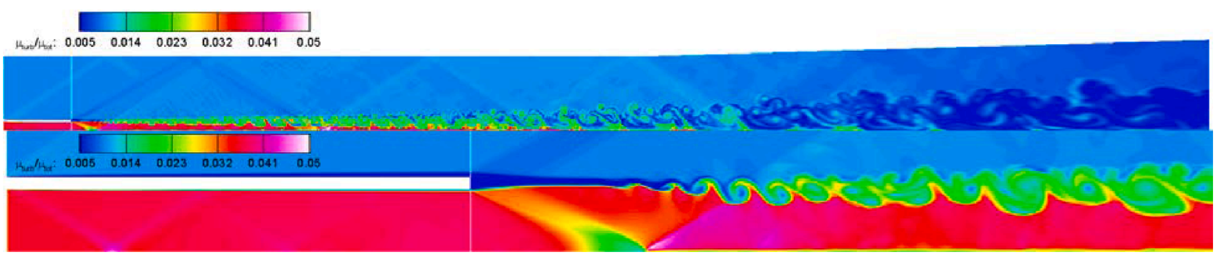

Fig. 23. Ratio of turbulent viscosity to the total viscosity in the flow field.

References

[1] Sutton GP, Biblarz O. Rocket propulsion elements. John Wiley & Sons 2016.
[2] Manski D, Goertz C, Saßnick H-D, Hulka JR, Goracke BD, Levack DJH. Cycles for earth-to-orbit propulsion. J Propul Power 1998;14(5):588–604.
[3] Yang V, Habiballah M, Hulka J, Popp M. Liquid rocket thrust chambers: aspects of modeling, analysis, and design. Prog Astronaut Aeronaut 2004;200.
[4] Dranovsky ML. Combustion instabilities in liquid rocket engines: testing and development practices in Russia. Prog Astronaut Aeronaut 2007;221.
[5] Yang V, Ku D, Walker M, Williams L, Leahy J. Liquid Oxygen/Kerosene Staged Combustion Rocket Engines with Oxidizer-Rich Preburners. NASA/TP 2015; 2015:218203.
[6] Yang V. Modeling of supercritical vaporization, mixing, and combustion processes in liquid-fueled propulsion systems. Proc Combust Inst 2000;28(1): 925–42.
[7] Hank J, Murphy J, Mutzman R. The X-51A scramjet engine flight demonstration program. 15th AIAA International Space Planes and Hypersonic Systems and Technologies Conference. 2008:2540.
[8] Seleznev R. History of scramjet propulsion development. J of Physics: Conf Series. 2018;1009:012028.
[9] Lin K-C, Jackson K, Behdadnia R, Jackson TA, Ma F, Yang V. Acoustic characterization of an ethylene-fueled scramjet combustor with a cavity flameholder. J Propul Power 2010;26(6):1161–70.
[10] Li J, Zhang L, Choi JY, Yang V, Lin K-C. Ignition transients in a scramjet engine with air throttling part 1: nonreacting flow. J Propul Power 2014;30(2):438–48.
[11] Li J, Zhang L, Choi JY, Yang V, Lin K-C. Ignition transients in a scramjet engine with air throttling part II: reacting flow. J Propul Power 2015;31(1):79–88.
[12] Micka DJ, Driscoll JF. Combustion characteristics of a dual-mode scramjet combustor with cavity flameholder. Proc Combust Inst 2009;32(2):2397–404.
[13] Koo H, Donde P, Raman V. LES-based Eulerian PDF approach for the simulation of scramjet combustors. Proc Combust Inst 2013;34(2):2093–100.
[14] Smart MK, Hass NE, Paull A. Flight data analysis of the HyShot 2 scramjet flight experiment. Aiaa J 2006;44(10):2366–75.
[15] Martinez Schramm J, Karl S, Hannemann K, Steelant J. Ground testing of the HyShot II scramjet configuration in HEG. 15th AIAA International Space Planes and Hypersonic Systems and Technologies Conference. 2008:2547.
[16] Won S-H, Jeung I-S, Parent B, Choi J-Y. Numerical investigation of transverse hydrogen jet into supersonic crossflow using detached-eddy simulation. Aiaa J 2010;48(6):1047–58.
[17] Fureby C, Chapuis M, Fedina E, Karl S. CFD analysis of the HyShot II scramjet combustor. Proc Combust Inst 2011;33(2):2399–405.
[18] Cecere D, Ingenito A, Giacomazzi E, Romagnoli L, Bruno C. Hydrogen/air supersonic combustion for future hypersonic vehicles. Int J Hydrogen Energ 2011;36(18):11969–84.
[19] Saghafian A, Terrapon VE, Pitsch H. An efficient flamelet-based combustion model for compressible flows. Combust Flame 2015;162(3):652–67.
[20] Waidmann W, Alff F, Bohm M, Brummund U, Clauss W, Oschwald M. Supersonic combustion of hydrogen/air in a scramjet combustion chamber. Space Technol 1995;15:421–9.
[21] Oevermann M. Numerical investigation of turbulent hydrogen combustion in a SCRAMJET using flamelet modeling. Aerosp Sci Technol 2000;4(7):463–80.
[22] Berglund M, Fureby C. LES of supersonic combustion in a scramjet engine model. Proc Combust Inst 2007;31(2):2497–504.
[23] Génin F, Menon S. Simulation of turbulent mixing behind a strut injector in supersonic flow. Aiaa J 2010;48(3):526–39.
[24] Shin J, Sung H-G. Zonal Hybrid Reynolds-Averaged Navier–Stokes/Large-Eddy Simulation of a Hydrogen-Fueled Scramjet Combustor. Aiaa J 2018;56(6): 2322–35.
[25] Burrows MC, Kurkov AP. An analytical and experimental study of supersonic combustion of hydrogen in vitiated air stream. AIAA Journal 1973;11(9):1217–8.
[26] Xiao X, Hassan HA, Baurle RA. Modeling scramjet flows with variable turbulent Prandtl and Schmidt numbers. Aiaa J 2007;45(6):1415–23.
[27] Edwards JR, Boles JA, Baurle RA. Large-eddy/Reynolds-averaged Navier-Stokes simulation of a supersonic reacting wall jet. Combust Flame 2012;159(3): 1127–38.
[28] Huang W, Wang Z-G, Li S-B, Liu W-D. Li S-b, Liu W-d. Influences of H2O mass fraction and chemical kinetics mechanism on the turbulent diffusion combustion of H2–O2 in supersonic flows. Acta Astronaut 2012;76:51–9.
[29] Vyasaprasath K, Oh S, Kim K-S, Choi J-Y. Numerical studies of supersonic planar mixing and turbulent combustion using a detached eddy simulation (DES) model. Int J Aeronaut Space 2015;16(4):560–70.
[30] Cao RR, Pope SB, Masri AR. Turbulent lifted flames in a vitiated coflow investigated using joint PDF calculations. Combust Flame 2005;142(4):438–53.

[31] Myhrvold T, Ertesvåg* IS, Gran IR, Cabra R, Chen J-Y. A numerical investigation of a lifted H2/N2 turbulent jet flame in a vitiated coflow. Combust Sci Technol 2006;178(6):1001–30.
[32] Patwardhan SS, De S, Lakshmisha KN, Raghunandan BN. CMC simulations of lifted turbulent jet flame in a vitiated coflow. Proc Combust Inst 2009;32(2):1705–12.
[33] Yang S, Wang X, Sun W, Yang V. Comparison of Finite Rate Chemistry and Flamelet/Progress-Variable Models: Sandia Flames and the Effect of Differential Diffusion. Combust Sci Technol 2020;192(7):1137–59.
[34] Evans JS, Schexnayder Jr CJ, Beach Jr HL. Application of a two-dimensional parabolic computer program to prediction of turbulent reacting flows. NASA STI/Recon Technical Report N 1978;78:20463.
[35] Cheng TS, Wehrmeyer JA, Pitz RW, Jarrett O, Northam GB. Raman measurement of mixing and finite-rate chemistry in a supersonic hydrogen-air diffusion flame. Combust Flame 1994;99(1):157–73.
[36] Evans JS, Schexnayder CJ. Influence of chemical kinetics and unmixedness on burning in supersonic hydrogen flames. Aiaa J 1980;18(2):188–93.
[37] Spiegler E, Wolfshtein M, Manheimer-Timnat Y. A model of unmixedness for turbulent reacting flows. Acta Astronaut 1976;3(3-4):265–80.
[38] Eklund DR, Drummond JP, Hassan HA. Calculation of supersonic turbulent reacting coaxial jets. Aiaa J 1990;28(9):1633–41.
[39] Jachimowski CJ. An analytical study of the hydrogen-air reaction mechanism with application to scramjet combustion. NASA Technical Paper 2791. 1988.
[40] Baurle RA, Alexopoulos GA, Hassan HA. Assumed joint probability density function approach for supersonic turbulent combustion. J Propul Power 1994;10(4):473–84.
[41] Zheng LL, Bray KNC. The application of new combustion and turbulence models to H2-air nonpremixed supersonic combustion. Combust Flame 1994;99(2):440–8.
[42] Norris J, Edwards J. Large-eddy simulation of high-speed, turbulent diffusion flames with detailed chemistry. 35th Aerospace Sciences Meeting and Exhibit. 1997:370.
[43] Balakrishnan G, Smooke MD, Williams FA. A numerical investigation of extinction and ignition limits in laminar nonpremixed counterflowing hydrogen-air streams for both elementary and reduced chemistry. Combust Flame 1995;102(3):329–40.
[44] Sabel'nikov V, Deshaies B, Figueira da Silva LF. Revisited flamelet model for nonpremixed combustion in supersonic turbulent flows. Combust Flame 1998;114(3-4):577–84.
[45] Balakrishnan G, Williams FA. Turbulent Combustion Regimes for Hypersonic Propulsion Employing Hydrogen-Air Diffusion Flames. J Propul Power 1994;10(3):434–7.
[46] Gerlinger P, Stoll P, Brüggemann D. An implicit multigrid method for the simulation of chemically reacting flows. J Comput Phys 1998;146(1):322–45.
[47] Gerlinger P, Möbus H, Brüggemann D. An implicit multigrid method for turbulent combustion. J Comput Phys 2001;167(2):247–76.
[48] Möbus H, Gerlinger P, Brüggemann D. Comparison of Eulerian and Lagrangian Monte Carlo PDF methods for turbulent diffusion flames. Combust Flame 2001;124(3):519–34.
[49] Mobus H, Gerlinger P, Bruggemann D. Scalar and joint scalar-velocity-frequency Monte Carlo PDF simulation of supersonic combustion. Combust Flame 2003;132:3–24.
[50] Baurle RA, Girimaji SS. Assumed PDF turbulence-chemistry closure with temperature-composition correlations. Combust Flame 2003;134(1-2):131–48.
[51] Davidenko D, Gökalp I, Dufour E, Magre P. Numerical simulation of hydrogen supersonic combustion and validation of computational approach. 12th AIAA International Space Planes and Hypersonic Systems and Technologies Conference. 2003:7033.
[52] Magre P, Bouchardy P. Nitrogen and hydrogen coherent anti-Stokes Raman scattering thermometry in a supersonic reactive mixing layer. Proc Combust Inst 2000;28(1):697–703.
[53] Mueller MA, Kim TJ, Yetter RA, Dryer FL. Flow reactor studies and kinetic modeling of the H2/O2 reaction. Int J Chem Kinet 1999;31(2):113–25.
[54] Dauptain A, Cuenot B, Poinsot TJ. Large eddy simulation of a supersonic hydrogen-air diffusion flame. Complex Effects in Large Eddy Simulation 2005;71:98.
[55] Yetter RA, Dryer FL, Rabitz H. A comprehensive reaction mechanism for carbon monoxide/hydrogen/oxygen kinetics. Combust Sci Technol 1991;79(1-3):97–128.
[56] George E, Magre P, Sabel'nikov V. Numerical simulation of self-ignition of hydrogen-hydrocarbons mixtures in a hot supersonic air flow. 42nd AIAA/ASME/SAE/ASEE Joint Propulsion Conference & Exhibit 2006;4611.
[57] George E, Magre P, Sabel'nikov V. Self-ignition of hydrogen-hydrocarbons mixtures in a hot supersonic confined coflow of air. AIAA/CIRA 13th International Space Planes and Hypersonics Systems and Technologies Conference. 2005:3393.
[58] Bivolaru D, Cutler A, Danehy P, Gaffney R, Baurle R. Spatially and Temporally Resolved Measurements of Velocity in a H2-Air Combustion-Heated Supersonic Jet. 47th AIAA Aerospace Sciences Meeting including The New Horizons Forum and Aerospace Exposition. 2009:27.
[59] Ó Conaire M, Curran HJ, Simmie JM, Pitz WJ, Westbrook CK. A comprehensive modeling study of hydrogen oxidation. Int J Chem Kinet 2004;36(11):603–22.
[60] Izard J-F, Lehnasch G, Mura A. A Lagrangian model of combustion in high-speed flows: Application to scramjet conditions. Combust Sci Technol 2009;181(11):1372–96.
[61] Keistler PG, Hassan HA. Simulation of supersonic combustion involving H2/air and C2H4/air. Aiaa J 2010;48(1):166–73.
[62] Gerlinger P, Nold K, Aigner M. Influence of reaction mechanisms, grid spacing, and inflow conditions on the numerical simulation of lifted supersonic flames. Int J Numer Meth Fl 2010;62:1357–80.
[63] Jachimowski CJ. An analysis of combustion studies in shock expansion tunnels and reflected shock tunnels. Office of Management, Scientific and Technical Information Program: National Aeronautics and Space Administration; 1992.
[64] Vajda S, Rabitz H, Yetter RA. Effects of thermal coupling and diffusion on the mechanism of H2 oxidation in steady premixed laminar flames. Combust Flame 1990;82(3-4):270–97.
[65] Marinov NM, Westbrook CK, Pitz WJ. Detailed and global chemical kinetics model for hydrogen. Transport phenomena in combustion 1996;1.
[66] Smith GP, Golden DM, Frenklach M, Moriarty NW, Eiteneer B, Goldenberg M, et al. GRI3.0 mechanism. http://www.me.berkeley.edu/gri_mech/1995.
[67] Koo H, Donde P, Raman V. A quadrature-based LES/transported probability density function approach for modeling supersonic combustion. Proc Combust Inst 2011;33(2):2203–10.
[68] Donde P, Koo H, Raman V. Supersonic combustion studies using a multivariate quadrature based method for combustion modeling. 20th AIAA Computational Fluid Dynamics Conference 2011;3215.
[69] Boivin P, Dauptain A, Jiménez C, Cuenot B. Simulation of a supersonic hydrogen–air autoignition-stabilized flame using reduced chemistry. Combust Flame 2012;159(4):1779–90.
[70] Boivin P, Jiménez C, Sánchez AL, Williams FA. An explicit reduced mechanism for H2–air combustion. Proc Combust Inst 2011;33:517–23.
[71] Gomet L, Robin V, Mura A. Influence of residence and scalar mixing time scales in non-premixed combustion in supersonic turbulent flows. Combust Sci Technol 2012;184(10-11):1471–501.
[72] Karaca M, Lardjane N, Fedioun I. Implicit large eddy simulation of high-speed non-reacting and reacting air/H2 jets with a 5th order WENO scheme. Comput Fluids 2012;62:25–44.
[73] Davidenko D, Gökalp I, Dufour E, Magre P. Systematic numerical study of the supersonic combustion in an experimental combustion chamber. 14th AIAA/AHI Space Planes and Hypersonic Systems and Technologies Conference. 2006:7913.
[74] Lu S, Fan J, Luo K. High-fidelity resolution of the characteristic structures of a supersonic hydrogen jet flame with heated co-flow air. Int J Hydrogen Energ 2012;37(4):3528–39.
[75] Li J, Zhao Z, Kazakov A, Dryer FL. An updated comprehensive kinetic model of hydrogen combustion. Int J Chem Kinet 2004;36(10):566–75.
[76] Jin T, Luo K, Lu S, Fan J. DNS investigation on flame structure and scalar dissipation of a supersonic lifted hydrogen jet flame in heated coflow. Int J Hydrogen Energ 2013;38(23):9886–96.
[77] Luo K, Jin T, Lu SQ, Fan JR. DNS analysis of a three-dimensional supersonic turbulent lifted jet flame. Fuel 2013;108:691–8.
[78] Moule Y, Sabelnikov V, Mura A. Highly resolved numerical simulation of combustion in supersonic hydrogen–air coflowing jets. Combust Flame 2014;161(10):2647–68.
[79] Ribert G, Bouheraoua L, Domingo P. Large-eddy simulation of a supersonic burner. 52nd Aerospace Sciences Meeting 2014;0311.
[80] Koo H, Raman V, Varghese PL. Direct numerical simulation of supersonic combustion with thermal nonequilibrium. Proc Combust Inst 2015;35(2):2145–53.
[81] Zhang L, Choi JY, Yang V. Supersonic combustion and flame stabilization of coflow ethylene and air with splitter plate. J Propul Power 2015;31(5):1242–55.
[82] Singh DJ, Jachimowski CJ. Quasiglobal reaction model for ethylene combustion. Aiaa J 1994;32(1):213–6.
[83] Bouheraoua L, Domingo P, Ribert G. Large-eddy simulation of a supersonic lifted jet flame: Analysis of the turbulent flame base. Combust Flame 2017;179:199–218.
[84] Almeida YPd, Navarro-Martinez S. Large Eddy Simulation of a supersonic lifted flame using the Eulerian stochastic fields method. Proc Combust Inst 2019;37(3):3693–701.
[85] Karaca M, Zhao S, Fedioun I, Lardjane N. Implicit large eddy simulation of vitiation effects in supersonic air/H2 combustion. Aerosp Sci Technol 2019;89:89–99.
[86] Choi J-Y, Ma F, Yang V. Combustion oscillations in a scramjet engine combustor with transverse fuel injection. Proc Combust Inst 2005;30(2):2851–8.
[87] Fureby C. Towards the use of large eddy simulation in engineering. Prog Aerosp Sci 2008;44(6):381–96.
[88] Kraichnan RH, Montgomery D. Two-dimensional turbulence. Two-Dimensional Turbulence Rep Prog Phys 1980;43(5):547–619.
[89] Tabeling P. Two-dimensional turbulence: a physicist approach. Phys Rep 2002;362:1–62.
[90] Menter FR, Kuntz M, Langtry R. Ten years of industrial experience with the SST turbulence model. Turbulence, heat and mass transfer 2003;4:625–32.
[91] Choi J-Y, Jeung I-S, Yoon Y. Numerical study of scram accelerator starting characteristics. Aiaa J 1998;36(6):1029–38.
[92] Choi J-Y, Jeung I-S, Yoon Y. Computational fluid dynamics algorithms for unsteady shock-induced combustion, part 1: validation. Aiaa J 2000;38(7):1179–87.
[93] Baurle RA, Edwards JR. Hybrid Reynolds-averaged/large-eddy simulations of a coaxial supersonic freejet experiment. Aiaa J 2010;48(3):551–71.
[94] Kumar PP, Kim K-S, Oh S, Choi J-Y. Numerical comparison of hydrogen-air reaction mechanisms for unsteady shock-induced combustion applications. J Mech Sci Technol 2015;29(3):893–8.

[95] Berglund M, Fedina E, Fureby C, Tegnér J, Sabel'nikov V. Finite rate chemistry large-eddy simulation of self-ignition in supersonic combustion ramjet. Aiaa J 2010;48(3):540–50.

[96] Fureby C. Comparison of flamelet and finite rate chemistry LES for premixed turbulent combustion. 45th AIAA Aerospace Sciences Meeting and Exhibit. 2007: 1413.

[97] Baudoin E, Yu R, Bai, Nogenmur KJ, Bai X-S, Fureby C. Comparison of LES models applied to a bluff body stabilized flame. 47th AIAA Aerospace Sciences Meeting Including The New Horizons Forum and Aerospace Exposition. 2009:1178.

[98] Ingenito A, Bruno C. LES of a supersonic combustor with variable turbulent Prandtl and Schmidt numbers. 46th AIAA Aerospace Sciences Meeting and Exhibit. 2008:515.

[99] Boles JA, Edwards JR, Baurle RA. Large-eddy/Reynolds-averaged Navier-Stokes simulations of sonic injection into Mach 2 crossflow. Aiaa J 2010;48(7):1444–56.

[100] van Leer B. Towards the ultimate conservative difference scheme. V. A second-order sequel to Godunov's method. J Comput Phys 1979;32(1):101–36.

[101] Liu X-D, Osher S, Chan T. Weighted essentially non-oscillatory schemes. J Comput Phys 1994;115(1):200–12.

[102] Kim KH, Kim C. Accurate, efficient and monotonic numerical methods for multi-dimensional compressible flows - Part II: Multi-dimensional limiting process. J Comput Phys 2005;208(2):570–615.

[103] Gerlinger P. Multi-dimensional limiting for high-order schemes including turbulence and combustion. J Comput Phys 2012;231(5):2199–228.

[104] Kindler M, Gerlinger P, Aigner M. Investigation of hybrid rans/les approaches for compressible high speed flows. 17th AIAA International Space Planes and Hypersonic Systems and Technologies Conference. 2011:2218.

[105] Seidl MJ, Aigner M, Keller R, Gerlinger P. CFD simulations of turbulent nonreacting and reacting flows for rocket engine applications. J Supercrit Fluids 2017;121:63–77.

[106] Kim S, Lee S, Kim KH. Wavenumber-extended high-order oscillation control finite volume schemes for multi-dimensional aeroacoustic computations. J Comput Phys 2008;227(8):4089–122.

[107] Choi J-Y, Jeung I-S, Yoon Y. Computational fluid dynamics algorithms for unsteady shock-induced combustion, part 2: comparison. Aiaa J 2000;38(7): 1188–95.

[108] Henrick AK, Aslam TD, Powers JM. Mapped weighted essentially non-oscillatory schemes: achieving optimal order near critical points. J Comput Phys 2005;207 (2):542–67.

[109] Kim J-H, Yoon Y, Jeung I-S, Huh H, Choi J-Y. Numerical study of mixing enhancement by shock waves in model scramjet engine. Aiaa J 2003;41(6): 1074–80.

[110] Kim KH, Kim C, Rho O-H. Methods for the accurate computations of hypersonic flows - I. AUSMPW+ scheme. J Comput Phys 2001;174(1):38–80.

[111] Peters N, editor. Turbulent Combustion. Cambridge University Press; 2000.

[112] Yamashita H, Shimada M, Takeno T. A numerical study on flame stability at the transition point of jet diffusion flames. Symp (Int) Combust 1996;26(1):27–34.

[113] Lu T, Yoo CS, Chen J, Law CK. Three-dimensional direct numerical simulation of a turbulent lifted hydrogen jet flame in heated coflow: a chemical explosive mode analysis. J Fluid Mech 2010;652:45–64.

[114] Hartl S, Geyer D, Dreizler A, Magnotti G, Barlow RS, Hasse C. Regime identification from Raman/Rayleigh line measurements in partially premixed flames. Combust Flame 2018;189:126–41.

[115] Butz D, Hartl S, Popp S, Walther S, Barlow RS, Hasse C, et al. Local flame structure analysis in turbulent CH4/air flames with multi-regime characteristics. Combust Flame 2019;210:426–38.

[116] Papamoschou D. Model for entropy production and pressure variation in confined turbulent mixing. Aiaa J 1993;31(9):1643–50.

[117] Huh H, Driscoll JF. Shock-wave-enhancement of the mixing and the stability limits of supersonic hydrogen-air jet flames. Symp (Int) Combust 1996;26(2): 2933–9.